Nanofabrication (2022) 7, 62-88
https://doi.org/10.37819/nanofab.007.186

eurasia

RESEARCH ARTICLE

Check for updates

Antibacterial and photocatalytic activity of undoped and (Ag, Fe) co-doped CuO nanoparticles via microwave-assisted method

***Naveen Thakur[1], Anu[1], Kuldeep Kumar[2], Vijay Kumar Thakur[3], Ashwani Kumar[4] and Sher Singh Samant[5]**

[1]*Department of Physics, Career point university, Hamirpur (HP) INDIA*
[2]*Department of Chemistry, Career point university, Hamirpur (HP) INDIA*
[3]*Head, Biorefining and Advanced Materials Research Centre@SRUC, Edinburgh UK*
[4]*Patanjali Herbal Research Department, Patanjali Research Institute, Haridwar, INDIA*
[5]*Director, Himalayan Forest Research Institute, Shimla (HP), INDIA*
**Corresponding author mail ID: naveenthakur2327@gmail.com*

ABSTRACT

Nanoparticles (NPs) are miniature materials ranging from 1 to 100 nm. The NPs have unique chemical and physical properties due to their shape, size and high surface area. This research paper gives a detailed summary of the synthesis, characterization and applications of undoped and (Ag, Fe) co-doped CuO NPs with a diverse concentration of Fe (0.02, 0.04, 0.06 and 0.08 M) at a constant concentration of Ag (0.02 M). X-ray diffractometer (XRD) results revealed average crystallite size of NPs varies in the range 13.10-24.98 nm. Scanning electron microscopy (FE-SEM) showed that the morphology of pure synthesized CuO NPs and Energy dispersive x-ray spectroscopy (EDX) recognized the presence of Ag, Fe elements in the CuO lattice. The particle size obtained by transmission electron microscope (HR-TEM) images was found in the range 19.73-21.47 nm. Cu-O bond stretching of NPs was also confirmed by Fourier Transform Infrared (FTIR) techniques. The values of direct and indirect band gap for CuO were found to be 1.41-1.54 eV and 0.69-1.51 eV respectively. Antibacterial activity for synthesized NPs tested against gram-negative and gram-positive pathogenic bacteria. The photocatalytic properties of synthesized NPs were investigated by monitoring the methyl orange/methylene blue degradation in ultraviolet visible spectroscopy (UV-Vis).

ARTICLE HISTORY

Received: 16-11-2021
Revised: 30-01-2022
Accepted: 1-02-2022

KEYWORDS

Nanoparticles (NPs)
Minimum Bactericidal Concentration (MBC)
Minimum Inhibitory Concentration (MIC)
Methyl Orange
Methylene Blue

1. Introduction

Copper oxide (CuO) is semiconducting in nature with a monoclinic structure and heaving several interesting features, including antimicrobial activity, high stability and excellent thermal conductivity [1]. It has many applications in various fields like batteries, catalysis, lithium batteries, supercapacitors, magnetic recording equipment, photodetectors and in many more fields, these properties have encouraged scientists to control its shape and size for high performance [2]. Copper-compounds are effective biocidal products; these are commonly used in pesticide formulations and applications related to health [3]. Consequently, the synthesis of CuO nanoparticles (NPs) becomes practical, fundamental importance and necessity.

There are distinct approaches such as solution combustion [1], co-precipitation [4], sol-gel [5],

microwave-assisted [6], sonochemical [7], spray pyrolysis [8], hydrothermal [9], spin-coated [10], silar [11] and solvothermal [12] for the synthesis of CuO nanoparticles (NPs). However, these methods are being contently used for the synthesis of NPs, but they have numerous disadvantages, like they require more reaction time, more energy and temperature. But, the microwave-assisted method is not explored at the high end to date. It is an extreme expected and efficient routine among the entire further conventional synthesis methods for the synthesis of NPs. This environmentally friendly technique allows great heating, which makes it possible to obtain an excellent quantity of product for the short period of the reaction. The key benefit of using microwave is heat creation inside the substance at a molecular level. Heat will be distributed quickly and similarly concerning conventional heating. Being more efficient in producing high quality with advanced properties, homogeneous, filtered materials, smaller particle sizes, low external energy and less time consumption [13, 14 and 15], this method was used for the preparation of NPs in this research paper. Kannan *et al.* have also used the same method for the preparation of CuO NPs [13]. Basith *et al.* have also made use of this method for demonstration of undoped and Cobalt-doped CuO NPs [0.5, 1.0, 1.5, and 2.0 at wt% of Cobalt (Co)] [6].

Copper (Cu) has possible three oxidation states, for example, Cu^{+}, $Cu^{2+,}$ Cu^{3+} and consequently, both types of electrons and hole doping mechanism is achievable on metal oxide NPs [16]. The controlled doping of transition metal ions into host materials (CuO) is dexterous towards modifying the electronic configuration of the host, which increases as conductivity and physical properties of synthesized NPs [17, 18]. Co-doping (two types of atoms) into semiconductor oxides has engrossed huge interest as it leads to advanced photocatalytic activity and specific character compared to single element doping [19]. Literature evident several research papers on changes associated because of doping/ co-doping of metals into CuO NPs, such as Co [6, 18], La [1], Ce [7], Mg [12], Ni [15], Mn [8, 11], Mo [17], ZrO_2 [19], Fe and (Fe, Co) [10], (Ag, Ni) [14] and Ni and (La, Ni) [16]. Basith *et al.* have demonstrated the influence of Ni doping on their optical properties of pure CuO nanostructures by using the microwave technique. They reported that the values of average crystallite size lie between 20-26 nm [15].Yakout *et al.* have synthesized undoped and (Mn, Co) co-doped CuO nanocrystals via co-precipitation routine. They found that after the Mn and Co ions co-doping, the undoped CuO morphology was modified from NPs to nanorod structure, respectively [20]. Khmissi *et al.* have also fabricated CuO films of various thicknesses, Ni-doped, and (La, Ni) co-doped films through a spin coating method and observed increasing quantity of coated layers as 2-8, the values of average crystallite size were increased from14.23-28.32 nm [16]. CuO NPs have high potential as antimicrobial agents because they possess extremely remarkable crystal morphologies and high surface areas. These NPs have a wide range of properties against fungi, viruses and mites from the soil and bacteria. CuO NPs break the cell membrane of bacteria and prevent their development [21]. The antibacterial activities of CuO NPs depend upon the stability, size and concentration of the NPs [14, 21 and 22]. They have investigated the antibacterial activity of CuO NPs against both Gram-positive (*S. aureus* and *B. subtilis*) and Gram-negative (*P. aeruginosa* and *E. coli*) bacteria [23]. Dadi *et al.* also studied the antimicrobial activity of Zinc Oxide and CuO NPs against *Pseudomonas aeruginosa*, *Escherichia coli* and *Staphylococcus aureus* microbes by well and disc diffusion methods [24].

CuO NPs are well thought-out as the most attractive photocatalyst for the photodegradation of organic pollutants owing to their low fabrication cost, high optical absorption and optimal optical band gap for visible driven photocatalytic activity [25]. Conversely, the agglomeration of NPs may be affects their photocatalytic activity due to the reduction in the generation of reactive oxygen species (ROS). Additionally, separations of photocatalysts and recovery from the solution have been found to be the main obstacles for industrial applications, considering additional cost and secondary pollution by the photocatalyst [26]. Therefore, the transition metal co-doped CuO NPs have gained significant research interest because of their rich involvement in numerous emerging fields. Additionally, these NPs have shown great potential to provide structural and functional tunability. In recent times, environmental-related applications have gained much attention in utilizing the full potential of these fabricated NPs. This article mainly reviews the influence of (Ag, Fe)

co-doping on the structural, optical properties, antibacterial activity and photocatalytic activity of CuO NPs [27]. Subsequently, various researchers have investigated the photodegradation activity by doping it with different elements. P. Kar *et al.* have studied excellent photocatalytic activity towards reduction of carcinogenic and mutagenic Cr (VI) to nontoxic Cr (III) and degradation of toxic dye methylene blue (MB) under visible light illumination [28]. Sharma *et al.* have synthesized the TiO_2 doped gum tragacanth cross-linked 2- hydroxyethyl methacrylate hydrogel composite. They also reported that nGumT-cl-HEMA/TiO_2 hydrogel composite removal efficiency was 99.3 % adsorbent dose = 90 mg, MG = 50 ppm, pH = 7, volume = 50 mL and time = 80 min [29]. P. Jain *et al.* have studied the photocatalytic activity of TiO_2 nanoparticles (NPs) in-situ synthesized on an activated carbon fibre (ACF) substrate [30]. N. Singh *et al.* have studied the TiO_2 nanoparticles incorporated over Mutton bone-derived hydroxyapatite (MBHA) via a simple sol-gel route and also reported their photocatalytic activity under MB dye [31].

Synthesis of undoped and co-doped CuO NPs via microwave-assisted method is reported significantly less in literature, especially with the exploration of bactericidal effect and photocatalytic activity. Keeping in view above factors, this research article is devoted to the creation of undoped and (Ag, Fe) co-doped CuO NPs, which have been prepared by using microwave-assisted method, and further, their photocatalytic activity was carried out by using methylene blue (MB)/methyl orange (MO) dyes under UV-Vis spectroscopy. Antibacterial properties of freshly prepared NPs have also been studied at different concentrations. Silver (Ag) was taken as one of the doping agents since the nature of Ag^+ ions link as simple matrices, its antibacterial properties [32] and iron (Fe) are used as another dopant in CuO NPs since its electronic configuration was half-filled to provide balanced sharing of electrons which increases the substitution of the energy system to facilitate its stability. The incorporation of iron (Fe) ions into the lattice provides shallow traps for photo-generated electrons that improve and separate charge and narrow the energy bandgap through a redshift in the absorption edge [33]. Doping intends to modify the structural properties of the material without changing its crystalline structure and enhance optical, physical and antibacterial properties. The modifications in antibacterial activities for freshly prepared NPs have also been studied against bacterial strains *Bacillus subtilis (MTCC 441)*, *Staphylococcus aureus (MTCC 737)*, *Escherichic coli (MTCC* 739) and *Pseudomonas aeruginosa (MTCC 1688)* cells.

2. Materials and Methods

2.1. Materials

Copper (II) acetate monohydrate ($Cu(CH_3COO)_2 H_2O$), potassium hydroxide (KOH) pellets, polyethylene glycol (PEG), Iron (II) chloride tetrahydrate ($FeCl_2.4H_2O$) and silver nitrates ($AgNO_3$) were purchased from Merck, India. Microorganism's *B. subtilis* (MTCC 441), *S. aureus* (MTCC 737), *E. coli* (MTCC 739), and *P. aeruginosa (*MTCC 1688) were purchased from the CSIR-Institute of Microbial Technology (CSIR-IMTECH), Chandigarh.

2.2. Equipment

The synthesized NPs were characterized by the following analysis such as crystal structure was analyzed by X-ray diffractometer Philips Rigaku corporation smart lab 9 KW rotating anode by using 2θ=20°-80°, for the target CuK_α radiation (k = 1.5418 Å) with a step 0.2. The detailed study of morphological structure and elemental composition of these NPs were recorded via scanning electron microscopy model: JFEI Company of USA (S.E.A.) PTE LTD Nova nano SEM-450 equipped with energy-dispersive X-ray spectroscopy (EDX). High-resolution transmission electron microscopy (HR-TEM) model: FEI company of USA, FP 5022/22-Tecnai G2 20 S-Twins) were investigated the real images of NPs. UV-Vis spectroscopy (Perkin Elmer, UV-2450) to measure the ultraviolet-visible absorption spectra of these NPs samples at 200-800 nm range. Fourier transform infrared (FTIR) spectrometer (model: Agilent Technologies, L1600312 spectrum TWOLITA/ZnSe) assured examining the prepared samples› characteristic vibrational modes at 4000-400 cm^{-1} range.

2.3. Synthetic Procedure

Undoped and (Ag, Fe) co-doped CuO ($Cu_{1-x-y} Ag_x Fe_y O$) NPs (x = 0.02 M and y = 0.02, 0.04,

0.06, 0.08 M) were synthesized via microwave-assisted method. Copper (II) acetate monohydrate ($Cu(CH_3COO)_2H_2O$), potassium hydroxide (KOH) pellets, polyethylene glycol (PEG), silver nitrate ($AgNO_3$) and Iron (II) chloride tetrahydrate ($FeCl_2.4H_2O$) of AR grades were used. For undoped CuO NPs, primarily the desired amount of copper (II) acetate monohydrate (Cu $(CH_3COO)_2$ H_2O) as dissolved in 100 mL of distilled water and magnetically stirred upto 20 minutes to obtain obvious transparent solution. 0.3 M potassium hydroxide (KOH) and 0.1 g of polyethylene glycol (PEG) solution were dissolved 100 mL of distilled water individually. Now, individually the prepared solutions of polyethylene glycol (PEG) and potassium hydroxide (KOH) were dropwise in addition to the above-fabricated solution which maintains pH 9. The co-dopants, $AgNO_3$ and $FeCl_2.4H_2O$ were added drop-wise to the above prepared solution under continuous stirring. The synthesized solution was kept in a domestic household microwave oven and exposed to microwave energy a 2.45 GHz with power of 800 W for 35 minutes. Initially, the solution gets boiled and undergoes dehydration, followed by decomposition with the evolution of gases. The obtained black colour precipitate samples were washed systematically with several times distilled water and ethanol to eliminate the ions possibly remaining in the final products. The synthesized sample was dried out in a hot air oven at 60□ C for 24 hours. Therefore, at the end of the reaction, various parameters like reaction weight percentage, colour and time of the fabricated samples were noted. Therefore, this procedure was repeated for synthesis of $Cu_{0.94}Ag_{0.02}Fe_{0.04}O$, $Cu_{0.92}Ag_{0.02}Fe_{0.06}O$ and $Cu_{0.90}Ag_{0.02}Fe_{0.08}O$ NPs. The crystal structure and many other properties of synthesized NPs were analyzed by using different techniques.

2.4. Antibacterial Activities

The antibacterial activities of synthesized NPs were studied via well diffusion method (NCCLS, 1993) [34].

2.4.1. Preparation of Inoculums

(4-5) bacterial strains isolated colonies of the identical morphological type were chosen on a nutrient agar plate culture and taken into a test tube containing 5-6 mL of Nutrient broth medium. This tube was incubated at 37°C for 24 h. The turbidity of these prepared inoculums was compared with 0.5 McFarland standards solution ($1\text{-}2\times10^8$ CFU/mL).

2.4.2. Well diffusion method

First of all, prepared Mueller Hinton agar (MHA) plates containing inoculums sterilized cotton swab were speckled over the whole surface of MHA plates. In MHA plates, the wells were made with the help of cork borer. Thus, the fabricated (Ag, Fe) co-doped CuO NPs solution (50, 25 and 10 mg/mL w/v) as overloaded into the wells, as well as these NPs plates, were incubated at 37°C for 24 h. Distilled water and ciprofloxacin (100 µg/mL w/v) were used for a negative and positive control. After incubation of these NPs plates, the zone of inhibition was measured using the Hi antibiotic zone scale.

2.4.3. Minimum inhibitory concentration (MIC)

MIC of fabricated NPs was analyzed through broth micro dilution method (CLSI, M7-A7, 2006) [35]. The colonies of bacterial strains had grown up in a nutrient broth medium at 37°C overnight. All the wells of the 96-well microtiter plate were filled with a 100 µL dual strength solution of Muller-Hinton broth (MHB). Then the freshly prepared (2X) 100 µL solution of these fabricated NPs was added to the first well, and also serial dilutions were made in the concentration range up to the 9^{th} well. The bacterial cultures suspensions (10 µL) were added to each well of a microtiter plate. The growth control well (containing MHB and inoculums) was taken as 10^{th} well growth control well, negative control (Containing MHB, inoculums and distilled water) as 11^{th} well and positive control (containing MHB, inoculums and standard drug ciprofloxacin) was regarded as 12^{th} well. MIC of the synthesized NPs was well-thought-out as the lowest concentration, which shows that visual inhibition of growth for the particular bacterial organisms.

2.4.4. Minimum Bactericidal Concentration (MBC)

MBC of these fabricated NPs were studied via spreading 10 µL suspension from every well of a 96-microtiter plate on a nutrient agar plate. These nutrient agar plates were incubated for 24 h at

37°C. Thus, the same procedure was also repeated for positive and negative control wells.

2.4.5 Photocatalytic activity

The photodegradation of methyl orange/ methylene blue dye is carried out by using NPs under ultraviolet-visible spectroscopy (UV-Vis). In this activity, both synthesized undoped and (Ag, Fe) co-doped CuO NPs were used for degradation. The 100 mL of solution (10 ppm of methyl orange/methylene blue) was investigated by 15 mg and 30 mg of undoped and (Ag, Fe) co-doped CuO NPs for 90/60 minutes. Thus, the decomposition of methyl orange/ methylene blue dye was studied by the degradation rate and identified the change in absorbance through a UV-Visible spectrophotometer.

3. Results and Discussions

3.1. XRD Analysis

The structural properties of undoped and (Ag, Fe) co-doped CuO NPs were studied by XRD in the range of 30° - 80° and are shown in Figure 1. The pronounced diffraction peaks in the XRD peaks were located at 2θ = 32.850°, 35.424°, 38.789°, 48.854°, 53.513°, 58.416, 61.767°, 66.152°, 68.482°, 72.867° and 75.197 which corresponding to (110), (002), (200), (-202), (020), (202), (-113), (-311), (220), (311) and (004) crystal planes. XRD peaks (002) and (200) had much stronger intensity than other peaks, which exhibit a preferred orientation. XRD patterns confirmed the monoclinic structure of synthesized NPs. The monoclinic structure of CuO NPs remained unchanged after the Ag and

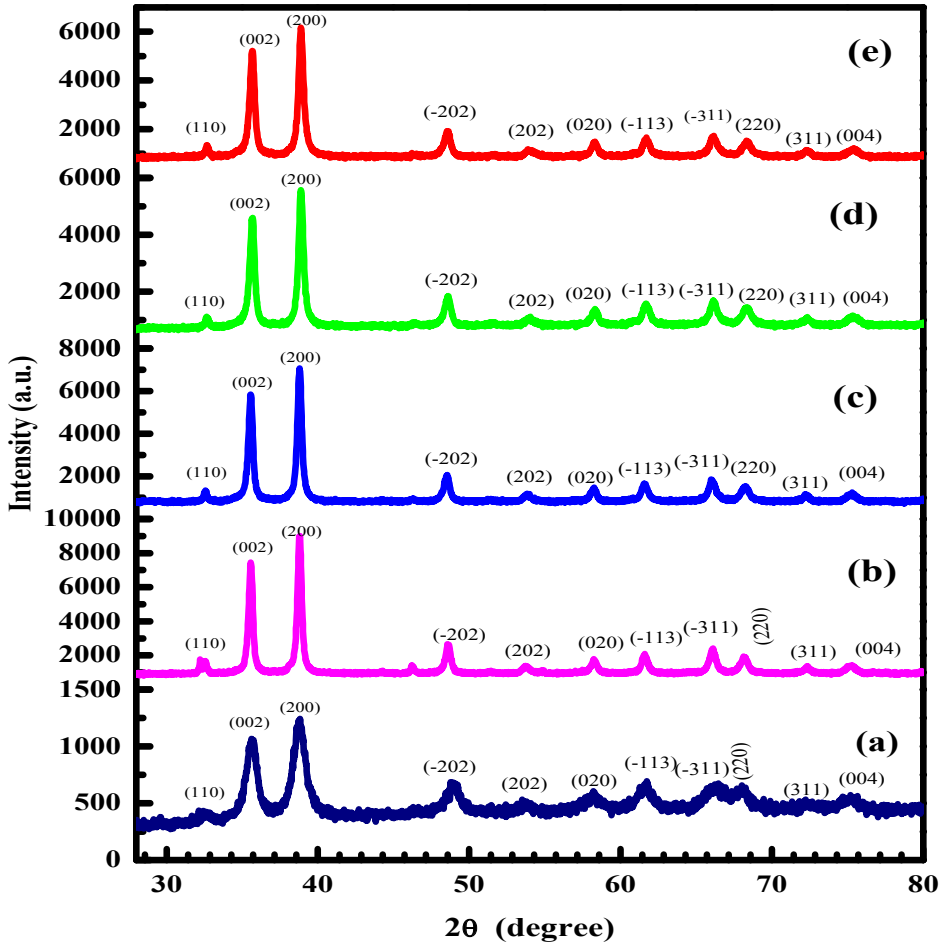

Figure 1. XRD spectra of **(a)** undoped and (Ag, Fe) co-doped CuO NPs with various concentrations of Fe content **(b)** 0.02, **(c)** 0.04, **(d)** 0.06 and **(e)** 0.08 M at same concentration of Ag content (0.02 M)

Fe co-doping. There are no specific changes in the peak arrangement. Additional peaks were recorded related to Ag and Fe ions in the co-doped CuO NPs because Ag and Fe atoms are efficiently substituted Cu sites within CuO lattice and do not influence the crystal structure of the parent substance (CuO). Analogous consequences were investigated for Co and (Co, Fe) co-doped CuO films spin-coated method [10] and also pure and (Mn, Co) co-doped CuO nanocrystals are prepared via co-precipitation routine [20]. The average crystallite size (D) of NPs was calculated by measuring the full width at the half-maximum (FWHM) of the most intense first three XRD diffraction planes by using the Debye-Scherrer formula given in equation (1) [14, 16].

$$D = \frac{0.94\lambda}{\beta cos\theta} \quad (1)$$

Whereas λ is the wavelength (λ = 1.546 Å), β is FWHM and θ is the angle of diffraction. These parameters of fabricated NPs are listed in Table 1. The average crystallite size for pure CuO NPs is 13.10 nm, whereas for (Ag, Fe) co-doped CuO NPs, the values were 24.98 nm, 22.26 nm, 17.88 nm and 19.17 nm. The values of average crystallite size of these NPs increased/decreased as the concentration of Fe ions increases due to an increase or decrease in crystallite size which were closely related to broadening or shrinking of the XRD peaks. The variation of size among pure and co-doped (Ag, Fe) NPs areas is probably owing to perceptive co-dopant incorporation in the arrangement of crystal structure and also resulted in altering the growth kinetics of crystal [19]. From table 1, it has been observed that the diameter of NPs increases then decreases with concentration of co-dopant, Fe. This is indicating a minor deterioration in the crystalline nature of NPs due to the incorporation of Fe ions in CuO crystal structure. The same trend was also reported by the researchers for co-doping of Ni and Ag to CuO in starting of the 2020 year [14]. The value of dislocation density was (δ) calculated via equation (2) given below [36].

$$\delta = \frac{1}{D^2} \quad (2)$$

The strain in terms of crystal defect and deformation-induced in powders was measured by Williamson-Hall (W-H) equations, and thus, the specified formula is given below.

$$\varepsilon = \frac{\beta}{4tan\theta} \quad (3)$$

By making use of strain values, stress was also calculated by using Hooke's law ($\sigma = C\in$), C = 1.46 ± 1010 N/m^2 whereas was the bulk Young's modulus [36]. The average crystallite size, strain (ε) stress (σ) and dislocation density (δ) for pure and (Ag, Fe) co-doped CuO NPs are listed in Table 1. The values of d-spacing, lattice parameter (a, b, c) and volume of the unit cell (V) were also calculated for NPs by using the following equations (4), (5) [14, 16] and are given in Table 1.

$$\frac{1}{d^2} = \frac{1}{sin^2\beta}\left[\frac{h^2}{a^2} + \frac{k^2}{b^2} + sin^2\beta\,\frac{l^2}{c^2} - \frac{2hlcos\beta}{ac}\right] \quad (4)$$

$$V = abcsin\beta \quad (5)$$

The volume of the unit cell (V) for undoped CuO NPs was 81.546 Å^3 and for (Ag, Fe) co-doped CuO NPs, it ranged from 81.760 to 81.195 Å^3. These changes in volume were due to two key points. First reason was the variation of ionic radius of Cu

NPs	D (nm)	Dislocation density (δ) 10^{-4} (nm^{-2})	$d_{spacing}$ [Å]			Lattice parameters			Strain (ε)	Stress (σ) (MPa)	Volume (Å)
			(110)	(002)	(200)	a[Å]	b[Å]	c[Å]			
CuO	13.10	58.271	2.763	2.521	2.318	4.64	3.47	5.06	0.476	695	81.546
$Cu_{0.96}Ag_{0.02}Fe_{0.02}O$	24.29	16.949	2.759	2.522	2.320	4.62	3.50	5.03	0.483	705	81.335
$Cu_{0.94}Ag_{0.02}Fe_{0.04}O$	17.34	33.258	2.745	2.520	2.321	4.64	3.48	5.04	0.487	711	81.381
$Cu_{0.92}Ag_{0.02}Fe_{0.06}O$	22.59	19.596`	2.731	2.507	2.309	4.61	3.54	5.01	0.489	713	81.760
$Cu_{0.90}Ag_{0.02}Fe_{0.08}O$	21.53	21.499	2.730	2.520	2.310	4.62	3.53	5.04	0.498	727	81.195

Table 1. Average crystallite size, dislocation density, d-spacing, lattice parameters, lattice strains, stress and volume of synthesized CuO NPs

(0.73 Å), Ag (1.26 Å), and Fe (0.64 Å) ions and the second reason was the variation of anisotropic in the CuO crystal arrangement. Now, stress and strain values for undoped and co-doped CuO NPs were lying in the array of 695-727 and 0.476-0.489, respectively. The calculated values of stress and strain increased as the doping of Fe content increased due to the atoms fascinated in non-equilibrium for a reason of altering microstructure and the shape of these NPs. Hence, the substitution of (Ag, Fe) ions into CuO lattice increased the stress and strain values for CuO NPs. The values of stress and strain are presented below in Table 1. The obtained values of these fabricated NPs are shown in good agreement with the reported values in the literature [10, 14, 16 and 36].

3.2. SEM analysis (Surface Morphology and Chemical Composition)

SEM images were accomplished to confirm the NPs morphology and nature, as illustrated in Figure 2. During SEM images, a signal was generated which produced a two-dimensional (2-D) pattern and gave the external morphology (texture) information of the sample and elemental composition, which was used with the EDS feature, also gave direction of resources building up the sample. The morphology of NPs was rod like for CuO {Figure 2(a)}, sheet and spherical were found of particles for $Cu_{0.96}Ag_{0.02}Fe_{0.02}O$ {Figure 2(b)}, sheet and rod like structure for$Cu_{0.94}Ag_{0.02}Fe_{0.04}O$ {Figure 2(c)}, agglomerated rod like structure for $Cu_{0.92}Ag_{0.02}Fe_{0.06}O$ and agglomerated spherical like structure for $Cu_{0.90}Ag_{0.02}Fe_{0.08}O$ {Figure 2(d) & (e)}. Moderate difference was observed in the morphology of undoped and co-doped CuO NPs. The average particle size of NPs was 16.53 nm, 25.855 nm, 27.800 nm, 28.640 nm, and 29.706 nm, respectively. Particle size of these NPs increased with the influence of co-doping of (Ag, Fe) ions on pure CuO NPs. The alterations in morphologies of synthesized NPs are associated with the growth process owing to the nucleation mechanism of the particles. For this reason, that of reserved nucleation rate and a consequent minor enlargement rate of NPs possibly emerge while the ionic radii of Ag^{+} and Fe^{2+} ions are diverse from that of Cu^{2+} ions [37]. The elemental composition of these fabricated samples was studied through energy dispersive X-ray (EDX) spectroscopy, as illustrated in Fig.2 (a), b, c, d, e). The EDX spectrums were analyzed at 20 keV. EDX spectra revealed that the samples were without any impurity. Figure 2 (a, b, c, d, e) established the element composition and weight percentage of Cu, Ag, Fe and O elements that are present in every fabricated co-doped CuO NPs, which were in agreement with the experiment and the obtained peaks at 2.10-2.25 KeV was owing to the existence of gold (Au), which was used for sample coating through SEM/EDX micrograph analysis [38].

3.3. HR-TEM Results

The HR-TEM patterns of undoped and (Ag, Fe) co-doped CuO NPs are given below in Figure 3. HR-TEM images predicted the actual size of these fabricated NPs. Figure 3(a) revealed the presence of ellipsoidal type shaped particles in ,the case of undoped CuO NPs owing to NPs aggregation. Figure 3(c) and (e) given sheet and nanoflakes like the structure of NPs and within the case of Figure 3(g) and (i) the particles due to sheet, shuttle and rod-like structure. It is clear from these Figures that undoped CuO NPs undergo a substantial alteration in morphologies as of ellipsoidal to rod-like structures consequential to co-doping with Ag and Fe ions. This morphological change was due to the presence of Ag and Fe ions in the solution through the preparation process. These images' average particle sizes were 20.55 nm, 22.30 nm, 19.73 nm, 21.474 nm and 20.45 nm. The size of $Cu_{0.94}Ag_{0.02}Fe_{0.04}O$ NPs and $Cu_{0.90}Ag_{0.02}Fe_{0.08}O$ NPs decreased as compared to undoped CuO NPs. But in case of $Cu_{0.96}Ag_{0.02}Fe_{0.02}O$ NPs and $Cu_{0.92}Ag_{0.02}Fe_{0.06}O$ NPs, the size increased as compared to undoped CuO NPs. Thus, in the case of (Ag, Fe) co-doped CuO, the recorded size of these fabricated NPs was slightly smaller than the (Ag, Ni) co-doped CuO NPs [14]. Therefore, the crystallite sizes obtained from the XRD data are smaller than the sizes calculated from HR-TEM. It is well-established fact that the particle size is obtained from the XRD data of one crystal, while TEM gives the particle size that may consist of more than one crystal. The same trends are reported for pure and (Mn, Co) co-doped CuO nanostructures [20].

Figure 3(b, d, f, h, j) showed the characteristic rings of selected area electron diffraction (SAED) images of undoped and (Ag, Fe) co-doped CuO NPs with varied concentrations. SAED images of synthesized NPs showed unusual spotted

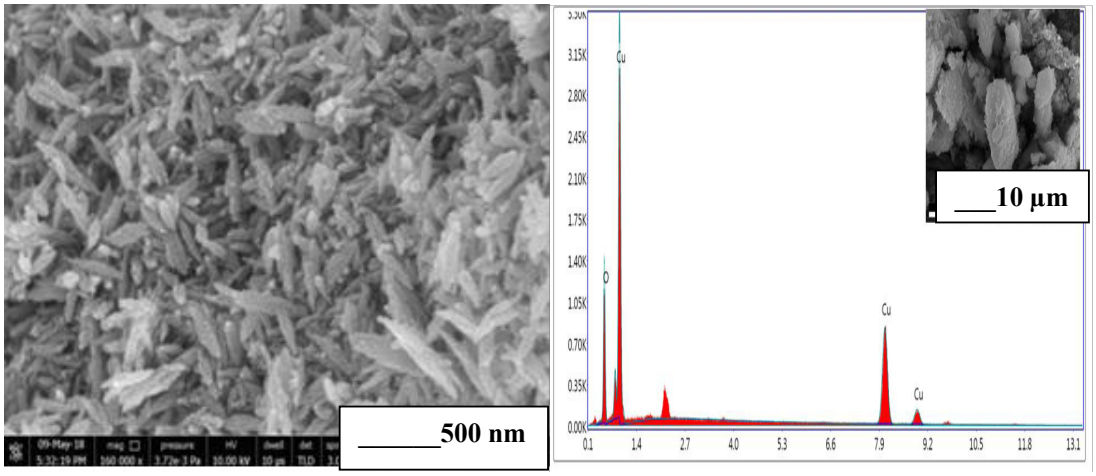

(a)

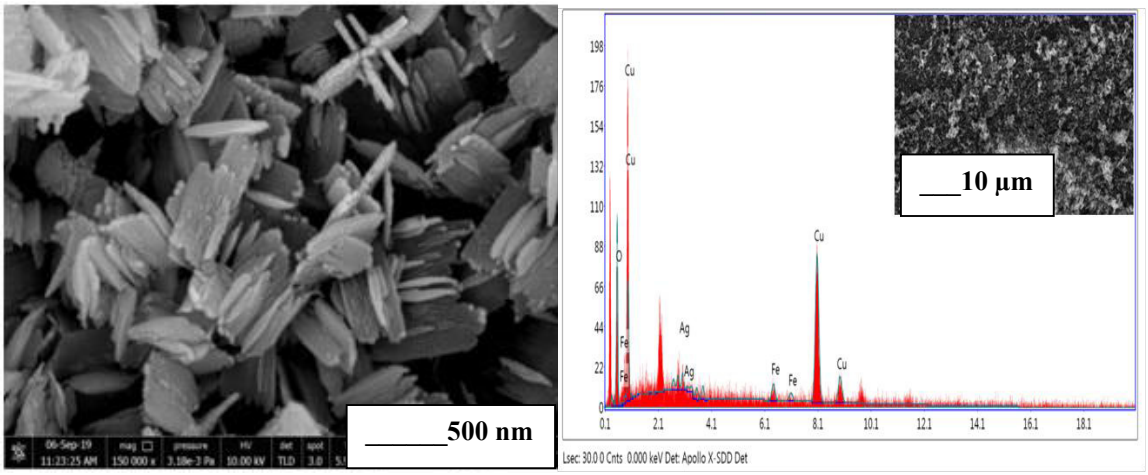

(b)

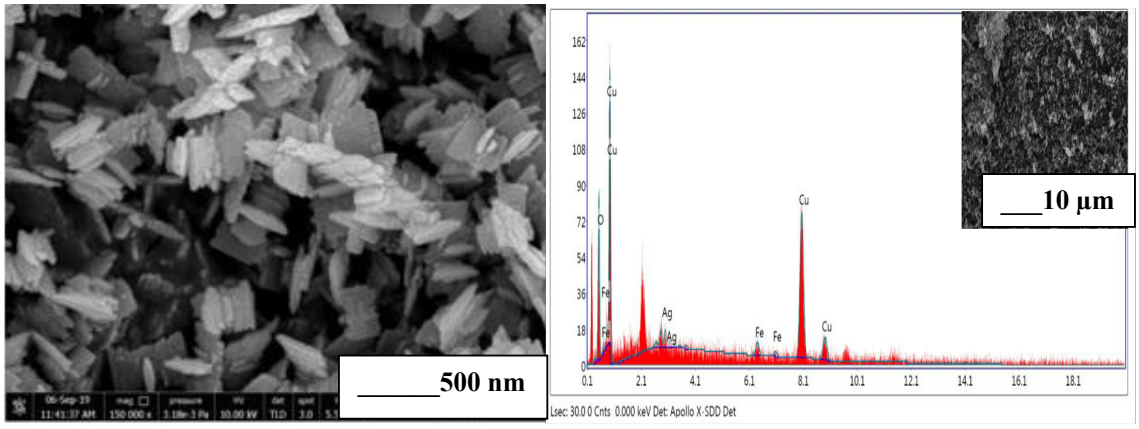

(c)

Figure 2. SEM/EDS patterns of **(a)** undoped CuO NPs at 500 nm, **(b)** $Cu_{0.96}Ag_{0.02}Fe_{0.02}O$ NPs at 500 nm, **(c)** $Cu_{0.94}Ag_{0.02}Fe_{0.04}O$ NPs at 500 nm, **(d)** $Cu_{0.92}Ag_{0.02}Fe_{0.06}O$ NPs at 500 nm, and **(e)** $Cu_{0.90}Ag_{0.02}Fe_{0.08}O$ NPs at 1 µm

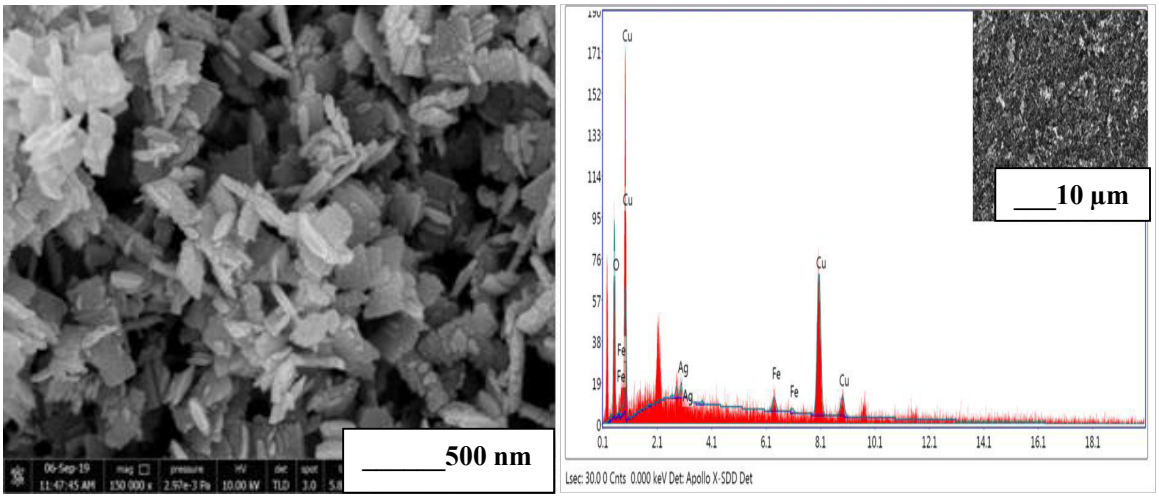

(d)

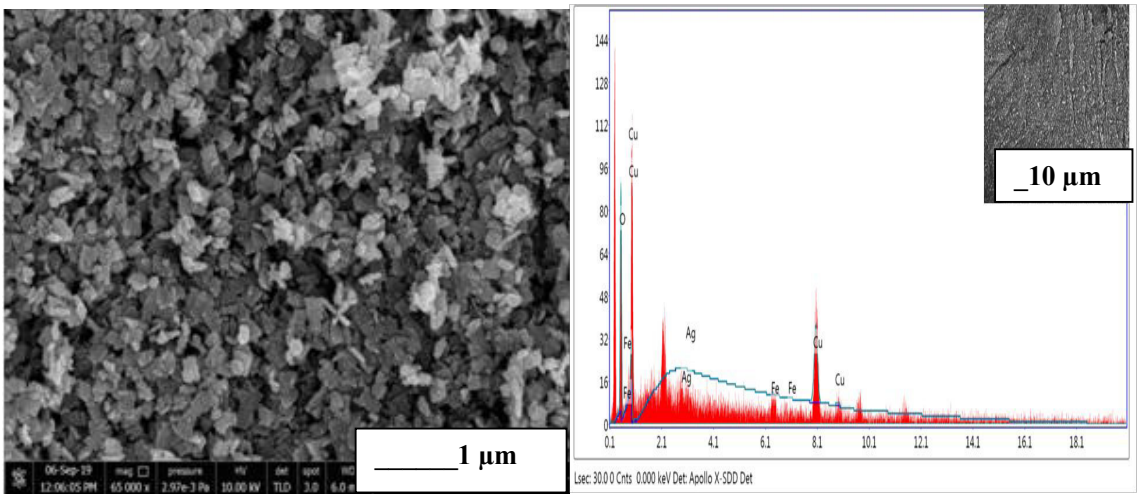

(e)

Figure 2 (*continued*). SEM/EDS patterns of **(a)** undoped CuO NPs at 500 nm, **(b)** $Cu_{0.96}Ag_{0.02}Fe_{0.02}O$ NPs at 500 nm, **(c)** $Cu_{0.94}Ag_{0.02}Fe_{0.04}O$ NPs at 500 nm, **(d)** $Cu_{0.92}Ag_{0.02}Fe_{0.06}O$ NPs at 500 nm, and **(e)** $Cu_{0.90}Ag_{0.02}Fe_{0.08}O$ NPs at 1 µm

concentric rings and the spots observed at varied orientations. The interplanar distances of undoped CuO NPs were established at d_1= 0.253 nm, d_2 = 0.236 nm, and d_3= 0.252 nm for the planes of crystal (110), (002), and (200) correspondingly. The interplanar distances of (Ag, Fe) co-doped CuO NPs of diverse concentration of Fe content at same concentration of Ag content revealed as d_1 = 0.252, 0.210, 0.248, 0.247 nm, d_2= 0.217, 0.173, 0.179, 0.270 nm and d_3= 0.178, 0.146, 0.156, 0.264 nm for the planes of crystal (110), (002), (200), (20-2), (202) and (11-3) simultaneously.

3.4. FTIR Results

The FTIR patterns of undoped and (Ag, Fe) co-doped CuO NPs with different concentration were recorded in the range 4000-400 cm^{-1} in powder form as shown in Figure 4. These samples assigned main three absorption peaks in the region of 400-4000 cm^{-1} because of Cu-O bond stretching vibrations. The peaks at 617.198-416.048 cm^{-1} for undoped CuO, 412.179-613.329 cm^{-1} for $Cu_{0.96}Ag_{0.02}Fe_{0.02}O$, 412.179-613.329 cm^{-1} for $Cu_{0.94}Ag_{0.02}Fe_{0.04}O$, 437.323-625.901 cm^{-1} for

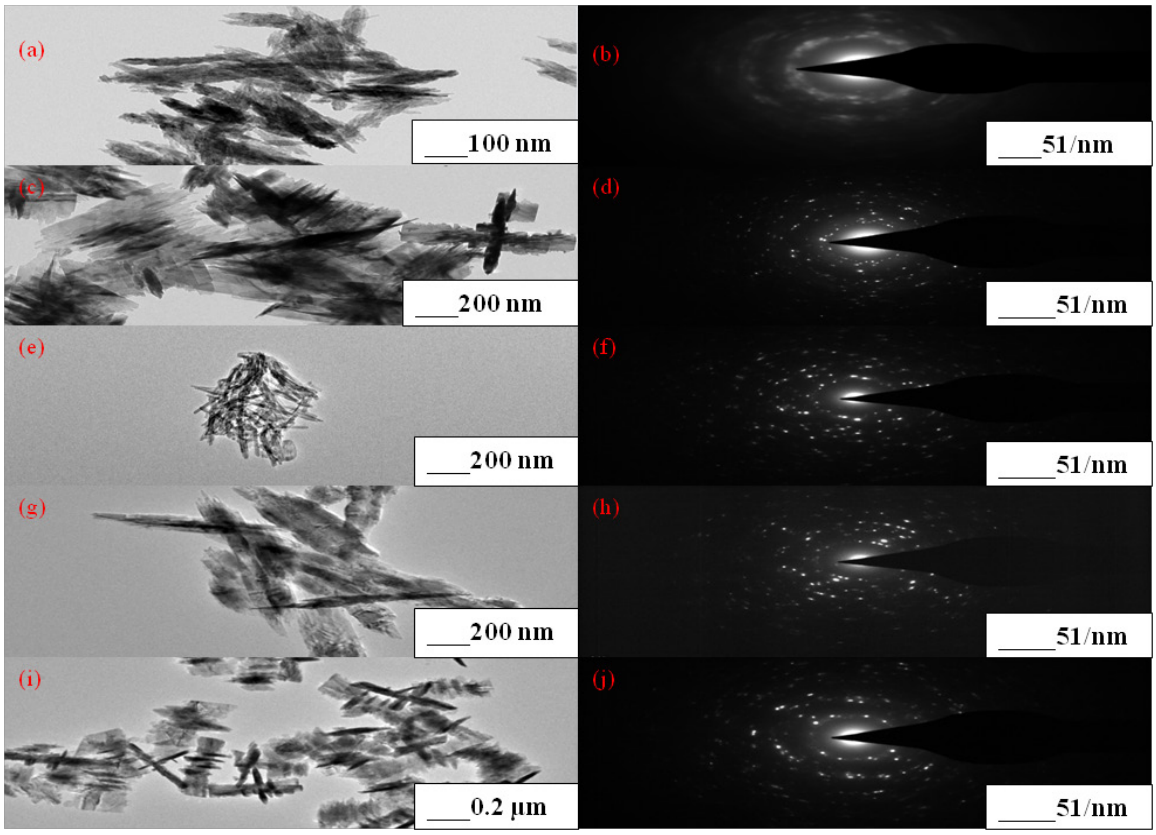

Figure 3. HR-TEM patterns **(a)** undoped CuO NPs at 100 nm, **(c)** $Cu_{0.96}Ag_{0.02}Fe_{0.02}O$ NPs at 200 nm, **(e)** $Cu_{0.94}Ag_{0.02}Fe_{0.04}O$ NPs at 200 nm, **(g)** $Cu_{0.92}Ag_{0.02}Fe_{0.06}O$ NPs at 0.2 µm **(i)** $Cu_{0.90}Ag_{0.02}Fe_{0.08}O$ NPs at 0.2 µm and SAED patterns **(b)** undoped CuO NPs at 51/nm, **(d)** $Cu_{0.96}Ag_{0.02}Fe_{0.02}O$ NPs at 51/nm, **(f)** $Cu_{0.94}Ag_{0.02}Fe_{0.04}O$ NPs at 51/nm, **(h)** $Cu_{0.92}Ag_{0.02}Fe_{0.06}O$ NPs at 51/nm, **(j)** $Cu_{0.90}Ag_{0.02}Fe_{0.08}O$ NPs at 51/nm

$Cu_{0.92}Ag_{0.02}Fe_{0.06}O$ and 412.179-625.901cm^{-1} for $Cu_{0.90}Ag_{0.02}Fe_{0.08}O$ were recognized toward Cu-O bond stretching.

Therefore, FTIR patterns also revealed the formation of Cu-O bonds in synthesized NPs. These obtained values showed good agreement with the literature [16]. The broad absorption band for synthesized NPs from 3437.166-3376.820 cm^{-1} was due to adsorbed water molecules. The material exhibits nano-crystalline nature owing to a high surface area-to-volume ratio and consequently, a high surface area-to-volume ratio absorbs moisture [20, 39]. The absorption band for undoped CuO NPs from 1445.239 cm^{-1} was due to O-H bending. The peaks obtained for doped NPs lied in the array 1406.325 cm^{-1} also confirmed to O-H stretching and 1579.430-1566.858 cm^{-1} due to carbohydrates to mixed modes [40]. Additional peak around 1579.430-1566.858 cm^{-1} was observed only in the case of doped NPs. This may be due to bond strength differences in the substitution of Cu^{2+} ions with Ag^{2+} and Fe^{2+} ions in CuO lattice structure. The minor shifting was observed within the peak arrangement of the absorption bands among (Ag, Fe) co-doped was due to the bond strength difference to the substitution of Ag^{2+} and Fe^{2+} for Cu ions in the CuO lattice structure and also revealed that the successful co-doping of Ag^{2+} and Fe^{2+} ions into CuO lattice. Absorption peaks related to the secondary phases were absent in the spectra.

3.5. UV-Vis spectroscopy Results

The UV-Vis absorption patterns of undoped and (Ag, Fe) co-doped CuO NPs were analyzed by UV-Vis-NIR spectrophotometry. Thus, the absorbance patterns were observed in the wavelength range as 200-800 nm and exposed below in Figure 5.

The direct band-gap values of prepared NPs were estimated by estimating the straight-line plot of

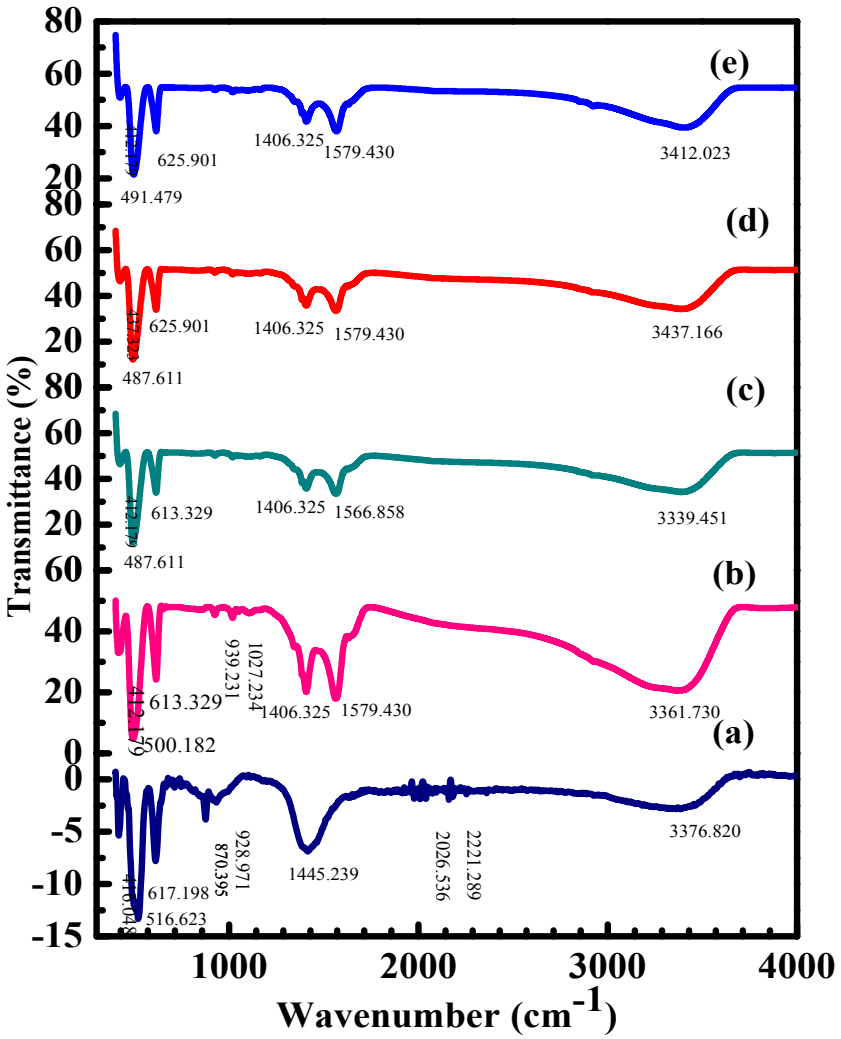

Figure 4. FTIR spectra **(a)** for undoped CuO NPs, **(b)** for $Cu_{0.96}Ag_{0.02}Fe_{0.02}O$ NPs **(c)** for $Cu_{0.94}Ag_{0.02}Fe_{0.04}O$ NPs, **(d)** for $Cu_{0.92}Ag_{0.02}Fe_{0.06}O$ NPs **(e)** for $Cu_{0.90}Ag_{0.02}Fe_{0.08}O$ NPs

photon energy (hν) vs $(\alpha h\nu)^2$ in Figure 6 {(a)-(e)} [19] and for indirect band-gap by interpolating the straight-line plot of the photon energy (hν) vs $(\alpha h\nu)^{1/2}$ in Figure 7 {(f)-(j)}. The relation between the absorption coefficients (α) and incidental photon energy also confide on the electronic transition types. Until electronic transitions, if the electron momentum is preserved, the conversion is direct. Although the momentum does not preserve, the transition is known as indirect. Electronic studies of these fabricated NPs were calculated by using the Kubelka-Munk equation {F(R)} such as [41].

$$F(R) = (1-R)^2/2R = \alpha/S \quad (6)$$

Wherever α is the absorption coefficient, and S is the dispersion factor, which is independent of the wavelength for particles, interrelated as the incidence photon energy. The ideal values of the optical band gap for undoped CuO and (Ag, Fe) co-doped CuO NPs were analyzed by using Tauc equation. The absorption spectra were also used to determine the bandgap values of CuO NPs throughout Tauc's equation as [42].

$$[\alpha h\upsilon]^n = B\,(h\upsilon - E_g) \quad (7)$$

Whereas B is a constant linked to the substance, h is Plank's constant, the photon energy is hυ in eV, υ is the photon frequency, E_g is the value of the optical band gap, n is an exponent factor whose values either 2 taken as for direct transition and ½ for an indirect transition.

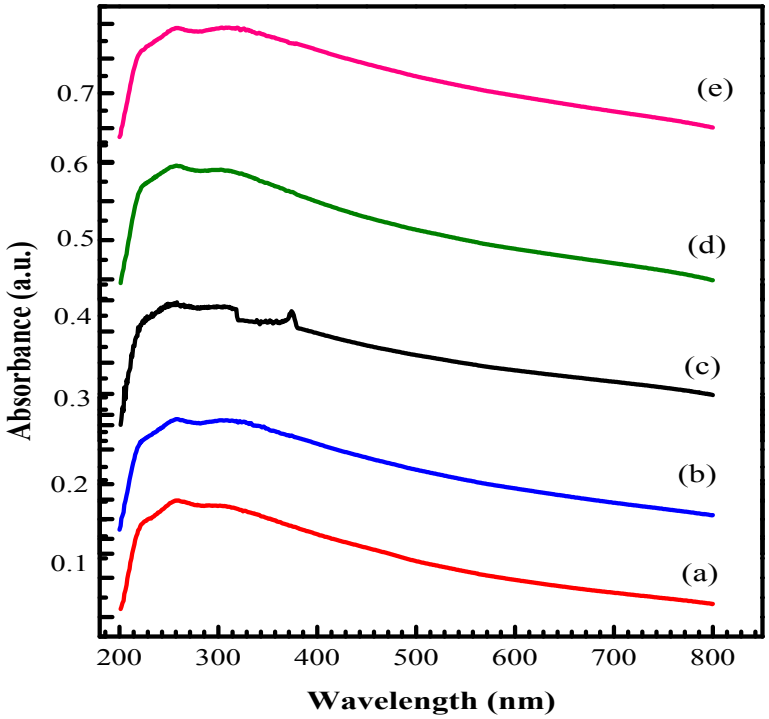

Figure 5. UV-Vis- NIR band of undoped **(a)** and **(b)-(e)** (Ag, Fe) co-doped CuO NPs with different concentration (0.02, 0.04, 0.06, 0.08 M) at taking constant silver concentration (0.02 M)

NPs Sample	Tauc relation for Direct Band Gap {(E_g(eV)}	Tauc relation for Indirect Band Gap {(E_g (eV)}
Undoped CuO	1.42	1.28
$Cu_{0.96}Ag_{0.02}Fe_{0.02}O$	1.45	1.04
$Cu_{0.94}Ag_{0.02}Fe_{0.04}O$	1.54	1.51
$Cu_{0.92}Ag_{0.02}Fe0_{.06}O$	1.54	0.69
$Cu_{0.90}Ag_{0.02}Fe_{0.08}O$	1.41	0.99

Table 2. Values of direct and indirect band gap {E_g (eV)} for undoped and (Ag, Fe) co-doped CuO NPs with different concentrations of Fe 0.02, 0.04, 0.06 and 0.08 M at same concentration of Ag (0.02 M).

The direct and indirect bandgap values were calculated from 1.41-1.54 eV and 0.69-1.51eV (Table 2). Therefore, researchers had also comprised the optical band gap values of CuO NPs [41]. S. Dhanuskodi *et al.* had investigated the values of indirect bandgap for pure and Fe (0.1wt% Fe, 0.3 wt% Fe) doped CuO NPs between 1.5eV-0.9 eV [42]. The optical band gap values may be decrease/increase for undoped CuO NPs due to the co-doping of Ag and Fe, which was due to the structural deformation. That possibly resolves the replacement of Cu ions in the CuO lattice by Ag and Fe ions. Therefore, the co-doping ions would take in a quantity of supplementary energy in the CuO band gap, which comes securely to the valence band edge.

This is due to the consequential diminution of the energy-related to the direct transition. Table 2 shows that the values of band gap for NPs are decreased considerably by increasing co-doping, which profits that co-doping may be used as a monitor for band gap values of CuO NPs. The band gap values of $Cu_{0.90}Ag_{0.02}Fe_{0.08}O$ are minimum due to carrier-carrier interaction and the significant distortion of the crystal lattice due to dopants [43]. Hence, the energy bandgap values strongly depend upon the

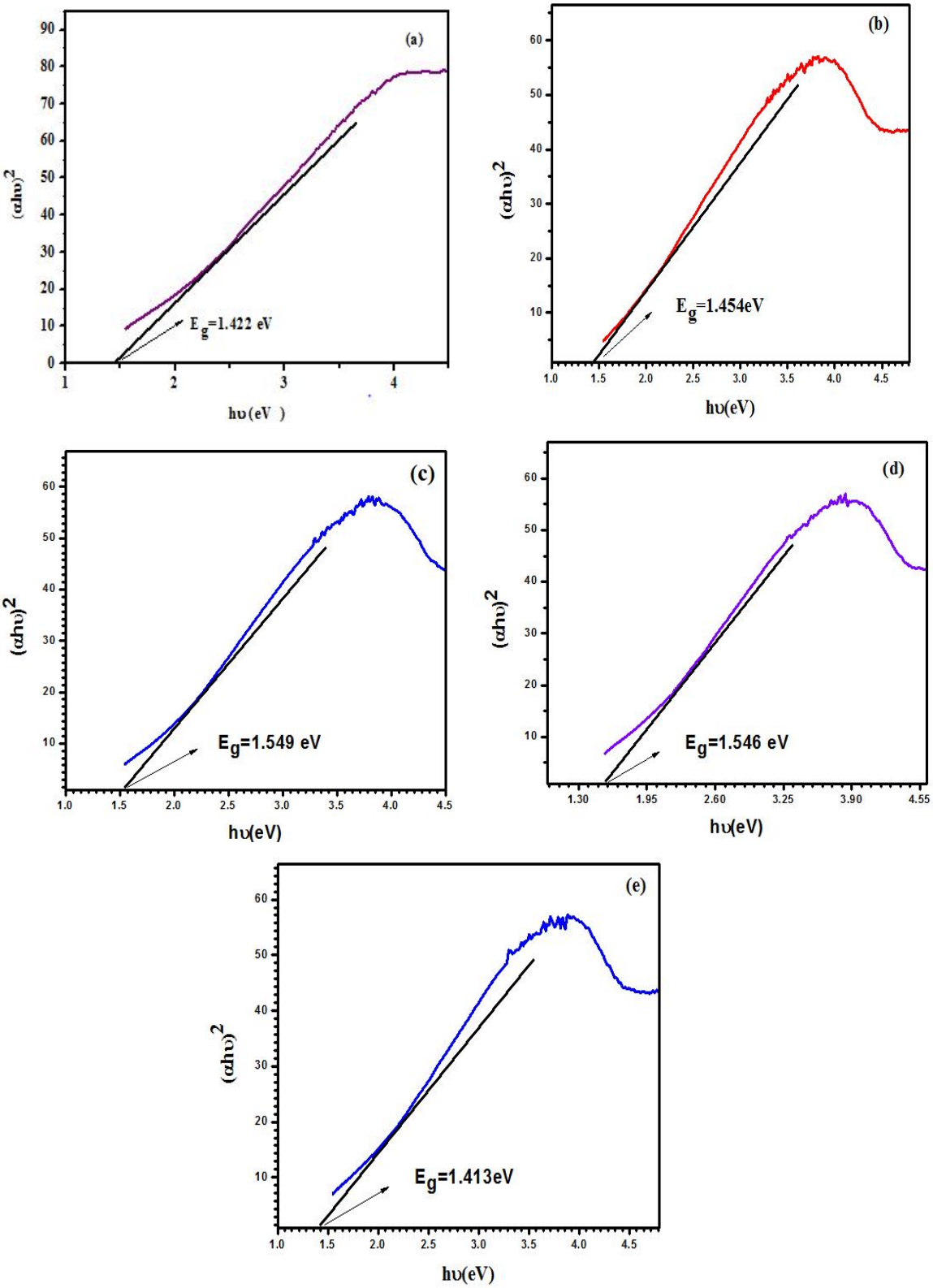

Figure 6. UV Visible spectrum of **(a)-(e)** direct band gap, from Tauc relation undoped and (Ag, Fe) co-doped CuO NPs with different concentrations of Fe (0.02, 0.04, 0.06 and 0.08M) at constant concentration of Ag (0.02M)

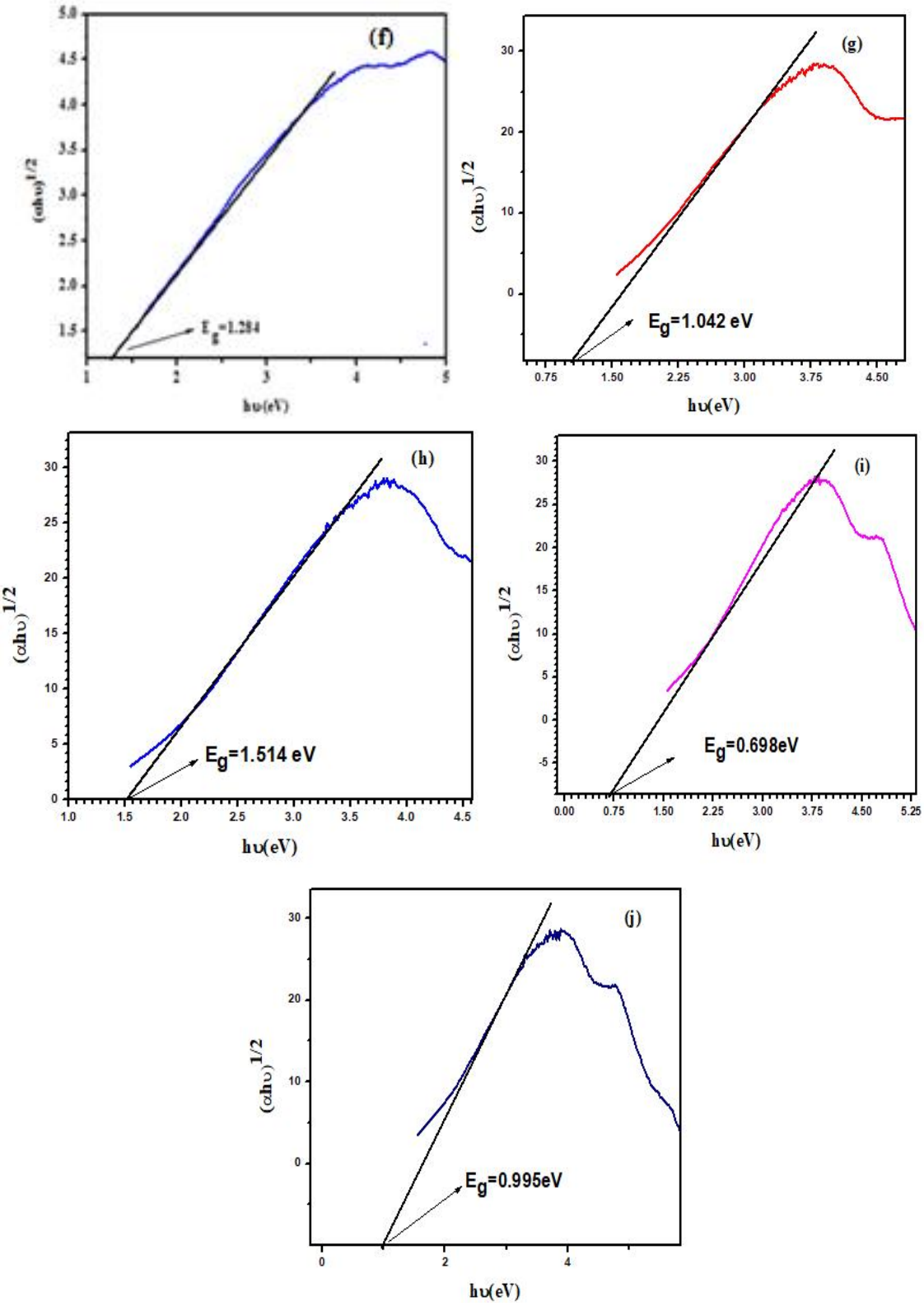

Figure 7. UV Visible spectrum of **(f)-(j)** indirect band gap from Tauc relation undoped and (Ag, Fe) co-doped CuO NPs with different concentrations of Fe (0.02, 0.04, 0.06 and 0.08M) at constant concentration of Ag (0.02M).

material's crystal structure, which in turn depends on the experimental conditions. Further, the band gap shrinkage occurs when the impurity or dopant concentration is particularly high. Therefore, the number of molecular orbitals, both bonding and antibonding, are increased, and the bandgap between valance and conduction band is decreased.

4. Antibacterial Activity

The antibacterial activity of freshly fabricated NPs against four pathogens such as *B. subtilis, S. aureus, E. coli* and *P. aeruginosa* were examined by Agar well diffusion routine. The antibacterial has been studied for 10, 25 and 50 mg/mL solutions of all samples of NPs in distilled water. Each well was loaded with 30 µL of solutions as taken as distilled water (negative control) and (100 µg/mL *w/v*) of ciprofloxacin (positive control). Figure 8 shows the inhibition of zones for fabricated NPs with different concentrations of NPs (10, 25 and 50 mg/mL) against pathogens such as gram-positive, gram-negative and ciprofloxacin as taken as positive control. The maximum zone inhibition

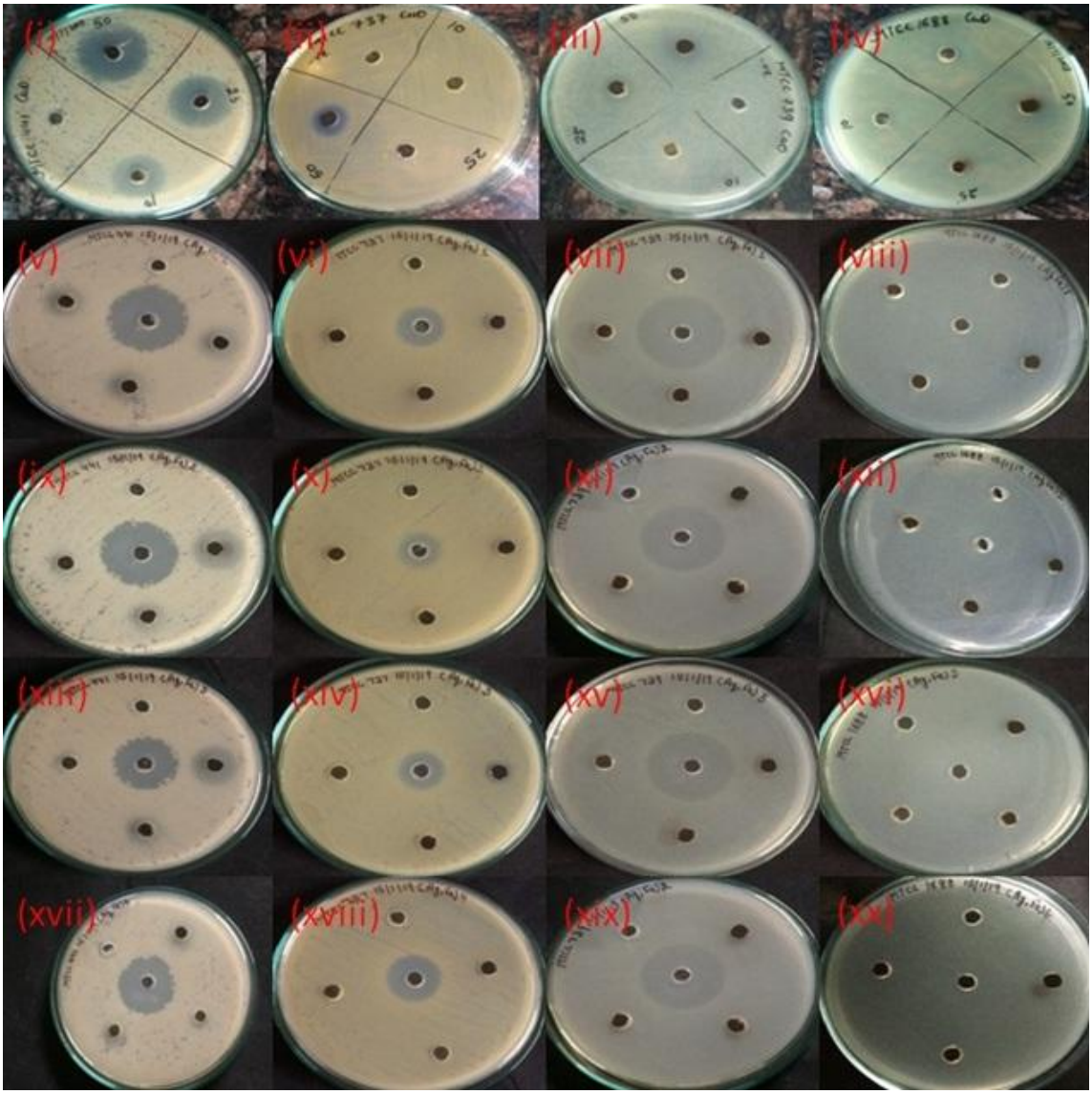

(a) **(b)** **(c)** **(d)**

Figure 8. inhibition of zones for (i-iv) undoped and (Ag, Fe) co-doped CuO NPs with different concentrations of Fe (v-viii) 0.02, (ix-xii) 0.04, (xiii-xvi) 0.06 and (xvii-xx) 0.08 M at same concentration of Ag content (0.02 M) against **(a)** *B. subtilis*, **(b)** *S. aureus*, **(c)** *E. coli* and **(d)** *P. aeruginosa*

was revealed for *Bacillus subtilis*, which was more significant than the following bacterial strains, such as *Escherichia coli*, *Staphylococcus aureus and Pseudomonas aeruginosa*.

The values for the zone of inhibition at different concentrations are given in Table 3. Synthesized undoped CuO NPs obtained with maximum zone of inhibition as compared to co-doped CuO NPs against *Bacillus subtilis.* In *Staphylococcus aureus,* co-doped CuO NPs showedshowed a zone of inhibition at all concentrations of NPs, but undoped CuO NPs showed activity only at 25 and 50 mg/mL concentrations. Results showed that among concentrations (10, 25, 50 mg/mL) tested at three concentrations levels of synthesized NPs, best growth inhibition is observed with 50 mg/mL concentration of $Cu_{0.94}Ag_{0.02}Fe_{0.04}O$ NPs against *S. aureus* (13.33±0.2) as compared to another co-doped CuO NPs. In *Escherichia coli,* co-doped CuO NPs ($Cu_{0.96}Ag_{0.02}Fe_{0.02}O$) showed the maximum inhibition zone than undoped CuO NPs. In case of $Cu_{0.96}Ag_{0.02}Fe_{0.02}O$ NPs with 50 mg/mL concentration of CuO NPs have showed top growth of inhibition against *E. coli* (14±0). In *Pseudomonas aeruginosa,* co-doped CuO NPs had shown no zone of inhibition compared to pure CuO NPs. *Pseudomonas aeruginosa* showed a zone of inhibition (12±0) at 50 mg/mL concentration for pure CuO NPs. This activity may depend upon a high surface to volume ratio and particle size. Generally, undoped CuO NPs showed a larger inhibition zone for many strains than other co-doped samples. $Cu_{0.94}Ag_{0.02}Fe_{0.04}O$ NPs showed the highest inhibition zone against *Staphylococcus aureus* strain and further increase of doping leads to decrease the inhibition zone. This is due to three factors that involved to showing increased antibacterial activity, i.e. increase in concentration, (Ag, Fe) co-doping and

NPs	NPs Conc. mg/mL	Bacterial strains			
		B. subtilis	***S. aureus***	***E. coli***	***P. aeruginosa***
		***IZD (mm) ± SD**			
CuO	10	20±0.22	0	0	0
	25	23±0.66	12±0	11.3±0.4	0
	50	25.6±0.3	15.4±0.6	13±0	12±0
$Cu_{0.96}Ag_{0.02}Fe_{0.02}O$	10	13 ±0	9.33±0.22	12±0	0
	25	14±0	10±0	13±0	0
Ciprofloaxcin	50	16±0	11±0	14±0	0
	0.1	27±0	17±0	29±0	0
$Cu_{0.94}Ag_{0.02}Fe_{0.04}O$	10	10±0	10.66±0.33	9±0	0
	25	13 ±0	12±0	12±0	0
Ciprofloaxcin	50	20±0	13.33±0.22	13±0	0
	0.1	28±0	16.3±0.4	18±0	0
$Cu_{0.92}Ag_{0.02}Fe_{0.06}O$	10	9±0	9.3±0.67	9±0	0
	25	14±0	10±0	10±0	0
Ciprofloaxcin	50	18.6±0.6	11±0	14±0	0
	0.1	24±0	18±0	29±0	0
$Cu_{0.90}Ag_{0.02}Fe_{0.08}O$	10	9±0	8±0	9±0	0
Ciprofloaxcin	25	12±0	9±0	10±0	0
	50	15±0	10±0	12±0	0
	0.1	26.6±0.3	19±0	29±0	0

*****IZD = Inhibition zone diameter, SD = Standard deviation

Table 3. The zones of inhibition of undoped and (Ag, Fe) co-doped CuO NPs at different concentrations against four microorganisms

NPs calcination in oxygen that lead to the NPs to show best antibacterial activity. Therefore, the results showed that higher dosage of NPs have maximum zone of inhibition of gram-positive and gram-negative bacterial strains. The standard antibiotic ciprofloxacin was used as a positive control. The inhibition of zone for positive control (Ciprofloxacin with 0.1 mg/mL concentration) are 16.3-29 mm for gram positive strains (*Bacillus subtilis, Staphylococcus aureus)* and gram negative strains (*Pseudomonas aeruginosa, Escherichic coli)*. These results exposed that the antibacterial activity of undoped CuO NPs has been improved through the co-doping of silver (Ag) and iron (Fe) ions in *S. aureus*. As a result, considering the action of mechanism and modality of the co-dopant silver {(Ag) and iron (Fe)} cause the great significance upon bacterial strains.

Many researchers have also reported the effect of different NPs to hamper the growth of divergent bacteria [44, 45]. This study indicated that the morphology of CuO NPs plays a significant impact on the bacterial strains. In the bactericidal process NPs join to bacterial cell membrane and due to electrostatic interaction between these particles and cell membrane, which was due to interruption of cell-wall and at last killing the pathogens [39, 46]. The antibacterial properties of NPs were dependent upon a variety of factors like intrinsic properties, physical-chemical properties, surface modification and bacterial strain, which influenced the toxicity of NPs. M. Saraf *et al.* have studied the 2D materials such as graphene/reduced graphene oxide (rGO), transition-metal dichalcogenides (TMDs)/ oxides (TMOs), layered double hydroxides (LDHs), and MXenes, which possess great potential for the development of ultrasensitive biosensors and infective antimicrobial agents to fight against various infections/diseases [47]. Z. Usmani *et al.* have investigated the developments in bio-based antimicrobial encapsulations as an effective assessment to prevent the development of COVID-19 virus on surfaces and also diminish its spread through surface contact. They also further develop strategies in material science to focus on contagious pathogens (viruses) in the future [48]. B. Balasubramaniam *et al.* have reported the antibacterial and antiviral materials of different materials, such as small-molecule organics, synthetic and biodegradable polymers, silver (Ag), Titanium Dioxide (TiO_2), and copper-derived chemicals. Therefore, surface protection mechanisms of the materials against the pathogen colonies are discussed in detail, highlighting the key differences that determine the parameters that govern the future enlargement of advanced antibacterial and antiviral materials and their surfaces [49].

MBC is the lowest concentration of a compound (mg/mL) that might kill more than 99 % of bacterial strains present, whereas MIC is the concentration wherever the solution showed turbidity. MIC is reciprocal of antibacterial activity as low MIC represented higher antibacterial activity. It is observed that both MIC and MBC have shown an inverse relationship between the particle size and activity. Minimum Inhibitory Concentration and Minimum Bactericidal Concentration values of fabricated NPs with various dosages were evaluated through 96th well microtiter plate routine. Table 4 shows the values of MIC and MBC values of synthesized CuO NPs. The MIC and MBC values ranged between 156.2-625 and

Bacterial strains	MIC and MBC of NPs (µg/mL)									
	CuO		$Cu_{0.96}Ag_{0.02}Fe_{0.02}O$		$Cu_{0.94}Ag_{0.02}Fe_{0.04}O$		$Cu_{0.92}Ag_{0.02}Fe_{0.06}O$		$Cu_{0.90}Ag_{0.02}Fe_{0.08}O$	
	MIC	MBC	MIC	MBC	MIC	MBC	MIC	MBC	MIC	MBC
Bacillus subtilis	312.5	2500	312.5	5000	625	2500	156.2	2500	625	5000
Staphylococcus aureus	390.6	3125	625	5000	625	5000	312.5	5000	625	2500
Escherichia coli	781.25	6250	312.5	2500	312.5	2500	156.2	2500	312.5	2500
Pseudomonas aeruginosa	390.6	3125	ND	ND	ND	ND	ND	ND	ND	ND

ND = Not Determined

Table 4. MIC and MBC of undoped and (Ag, Fe) co-doped CuO NPs against four different strains.

2500-5000 µg/mL (depending on the particular bacterial strain), respectively. Gram-negative bacterial strains such as *S. aureus* (MIC: 625 µg/mL and MBC: 5000 µg/mL) and *P. aeruginosa* (MIC: 390.6 µg/mL and MBC: 3125 µg/mL). E. coli (MIC: 625 µg/mL and MBC: 5000 µg/mL) is more resistant than Gram-positive bacterial strains especially, *B. subtilis* (MIC: 625 µg/mL and MBC: 5000 µg/mL) and *S. aureus* (MIC: 625 µg/mL and MBC: 5000 µg/mL).

The antibacterial activities of Gram-positive and Gram-negative bacteria are mostly reported in the literature [44, 45]. These bacterial strains have a chemical composition and diverse structures in their cell wall. The outer membrane of Gram-positive bacteria is different from Gram-negative bacteria. Gram-negative bacteria have peptidoglycan in their outer layer, so they show staining and also helpful for protection from outer substances, while this layer was absent in Gram-positive bacteria. Different mechanism of CuO powders as an antibacterial agent has been studied numerous times [39]. This action of co-doped CuO NPs is due to the release of Ag^{+} and Fe^{2+} ions or these NPs due to penetration by the destruction of the cell membrane. This action might be present due to the formation of oxidative species from the surface of CuO NPs. The metal surfaces (with positive charge) assist in binding with the negative surface part of bacterial strains and improve the antibacterial effect [46] or it is due to the ability of Ag and Fe co-doped CuO NPs to break the cell membrane of pathogens by stimulating pits and gaps [39,44]. The proper function of the outer cell well is helped by bacterial proteins and cytoplasm. Thus, the Ag^{+} and Fe^{2+} ions interact with disulphide or sulfhydryl groups present in the enzyme and can cause cell death [41]. Therefore, it increases the co-doping concentrations, which increases the surface area of NPs and enhances antibacterial properties.

5. Photocatalytic activity

5.1 Photocatalytic Degradation of Methyl Orange (MO) dye

The photocatalytic activity of undoped and (Ag, Fe) co-doped CuO NPs with different concentration of Fe (0.02, 0.04, 0.06 and 0.08 M) at the same concentration of Ag content (0.02 M) were studied by the degradation of 100 mL of 10 ppm methyl orange (MO) dye in the existence of UV light for 90 minutes. The UV light plays an essential role in the degradation of dye, and this is identified as a colorless dye solution in the occurrence of undoped and (Ag, Fe) co-doped CuO NPs. The degradation percentage of methyl dye was intended by following equation (8).

$$\text{Percentage Degradation} = \frac{A_0 - A}{A_0} \times 100 \quad (8)$$

Anywhere A_o is the absorbance of pure dye solution; A is the absorbance of the reaction mixture at a time t [50]. The catalytic efficiency of pure and (Ag, Fe) CuO NPs are evaluated by plotting decomposition (A_o/A) vs reaction time in Figure 9 (b, d). Figures 9 (a, c) display the absorption spectra of the dye in the existence of fabricated samples of NPs for a particular instant interval since a preferred interval of time for the irradiation procedure. At irradiation instant, the degradation percentage of MO dye by 15 mg and 30 mg of undoped and (Ag, Fe) co-doped CuO NPs under UV light is given in Table 5. Furthermore, Figure 9 (a, c)

NPs	% Degradation	
	MO dye (15 mg)	MO dye (30 mg)
CuO	83%	85%
$Cu_{0.96}Ag_{0.02}Fe_{0.02}O$	73%	75%
$Cu_{0.94}Ag_{0.02}Fe_{0.04}O$	82%	84%
$Cu_{0.92}Ag_{0.02}Fe_{0.06}O$	77%	79%
$Cu_{0.90}Ag_{0.02}Fe_{0.08}O$	80%	81%

Table 5. Percentage Degradation of MO dye with undoped and (Ag, Fe) co-doped CuO NPs at different concentrations.

shows the comparison of the photocatalytic performance of different photocatalysts under UV light irradiation. Pure CuO NPs have exhibited very high performance under UV light irradiation. After co-doping on CuO with (Ag, Fe), the photocatalytic activity of the NPs was not significantly enhanced. The pure CuO NPs sample has shown the best performance, which demonstrated 85% degradation of MO dye after 90minofirradiation.Thus,$Cu_{0.96}Ag_{0.02}Fe_{0.02}O$doped CuO has demonstrated a higher photocatalytic activity than all other concentration of co-doped CuO NPs. Furthermore, $Cu_{0.94}Ag_{0.02}Fe_{0.04}O$, $Cu_{0.92}Ag_{0.02}Fe_{0.06}O$ and $Cu_{0.90}Ag_{0.02}Fe_{0.08}O$ NPs sample showed a lower percentage of degradation of MO dye than $Cu_{0.96}Ag_{0.02}Fe_{0.02}O$ NPs sample.

5.2 Photocatalytic Degradation of Methyl Blue (MB) dye

The photocatalytic activity of undoped and (Ag, Fe) co-doped CuO NPs with unlike concentrations

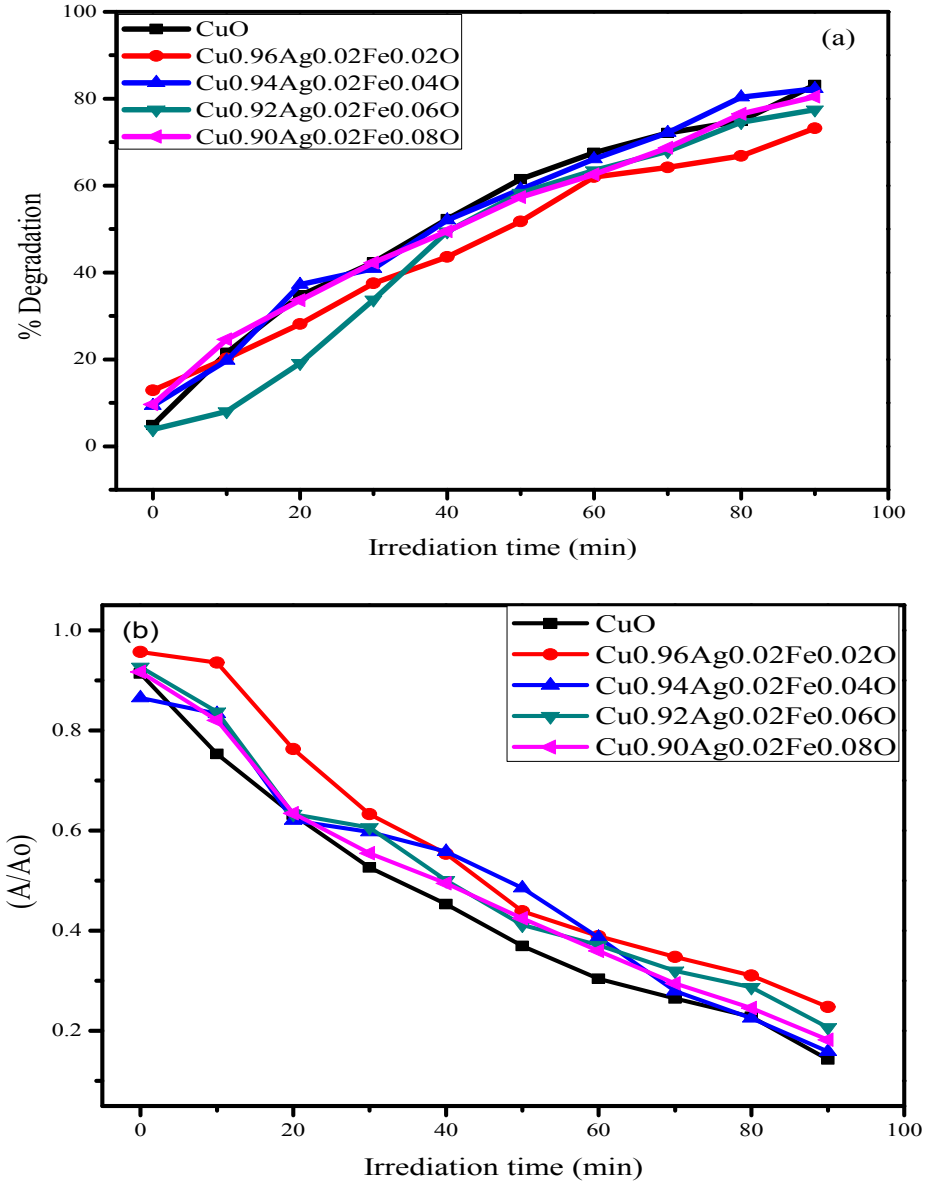

Figure 9. Percentage degradation **(a, c)** and catalytic efficiency **(b, d)** of undoped and (Ag, Fe) co-doped CuO NPs with different concentration of Fe (0.02, 0.04, 0.06 and 0.08 M) at same concentration of Ag (0.02 M).

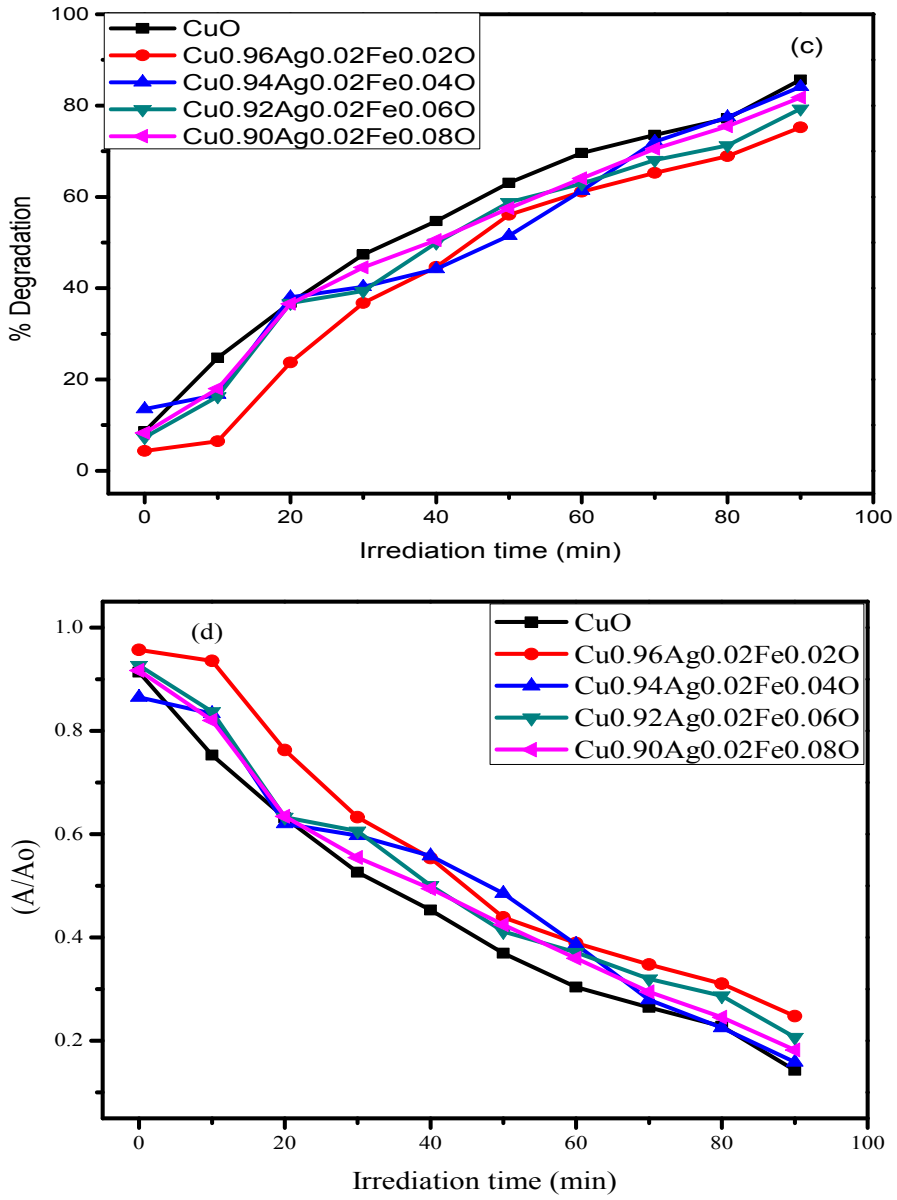

Figure 9 (*continued*). Percentage degradation **(a, c)** and catalytic efficiency **(b, d)** of undoped and (Ag, Fe) co-doped CuO NPs with different concentration of Fe (0.02, 0.04, 0.06 and 0.08 M) at same concentration of Ag (0.02 M).

of Fe (0.02, 0.04, 0.06 and 0.08 M) at taking the same concentration of Ag content (0.02 M) were studied by degradation of 100 mL of 10 ppm methyl blue (MB) dye in the incidence of UV light for 90 minutes. For degradation of MB dye and other calculations, the same procedure was adopted as for degradation of MO dye followed in section 5.1. The degradation percentage of MB dye by 15 mg and 30 mg of undoped and (Ag, Fe) co-doped CuO NPs under UV light is given in Table 6. Furthermore, the Figure 10 (a, c) shows the comparison of the photocatalytic performance of different photocatalysts under UV light irradiation. Pure CuO NPs have exhibited very high performance under UV light irradiation. After co-doping on CuO with (Ag, Fe), the photocatalytic activity of the NPs was not significantly enhanced. The pure CuO NPs sample has shown the best performance, which demonstrated 85% degradation of MB dye after 60 min of irradiation. Thus, $Cu_{0.96}Ag_{0.02}Fe_{0.02}O$ doped has demonstrated a higher photocatalytic

NPs	% Degradation	
	MB dye (15 mg)	MB dye (30 mg)
CuO	96%	97%
$Cu_{0.96}Ag_{0.02}Fe_{0.02}O$	91%	93%
$Cu_{0.94}Ag_{0.02}Fe_{0.04}O$	95%	96%
$Cu_{0.92}Ag_{0.02}Fe_{0.06}O$	92%	93%
$Cu_{0.90}Ag_{0.02}Fe_{0.08}O$	93%	94%

Table 6. Percentage Degradation of MB dye with undoped and (Ag, Fe) co-doped CuO NPs at different concentrations.

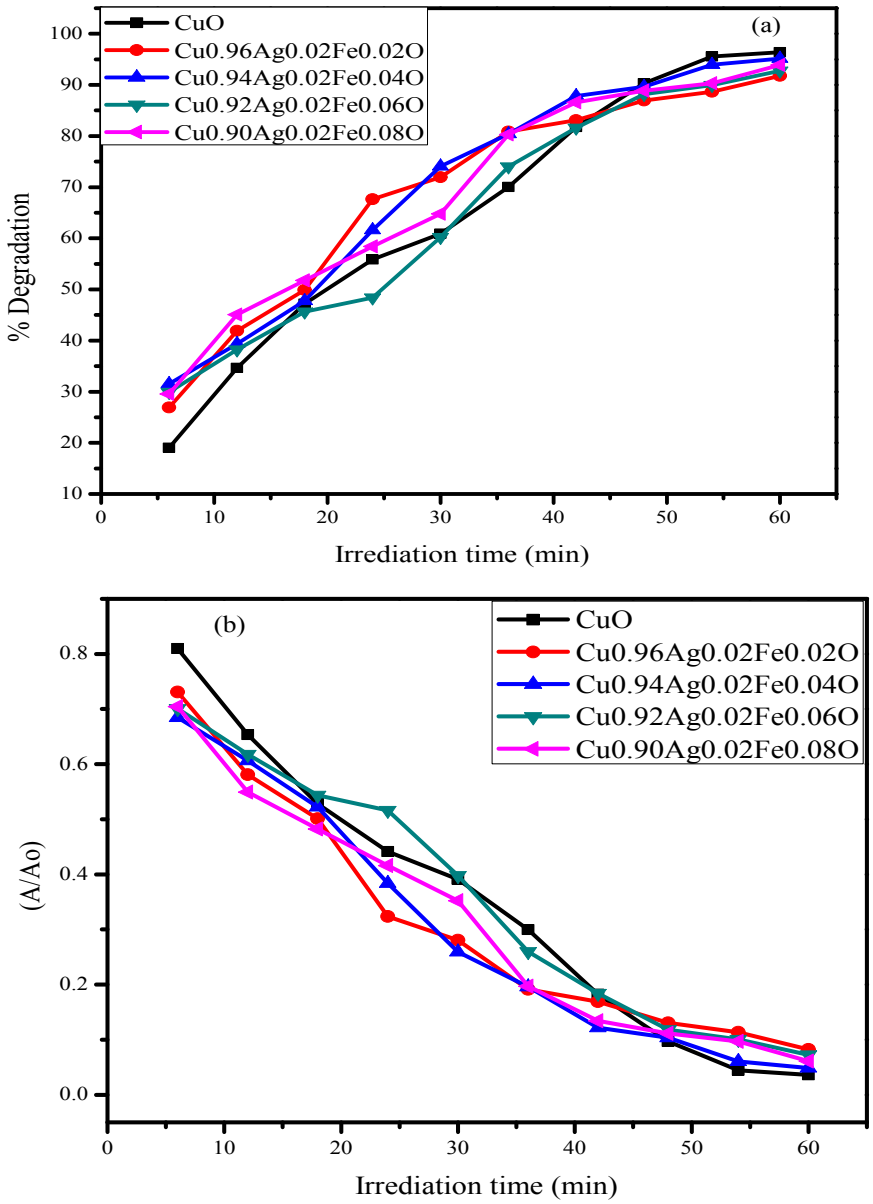

Figure 10. Percentage degradation **(a, c)** and catalytic efficiency **(b, d)** of undoped and (Ag, Fe) co-doped CuO NPs with different concentration of Fe (0.02, 0.04, 0.06 and 0.08 M) at same concentration of Ag content (0.02 M).

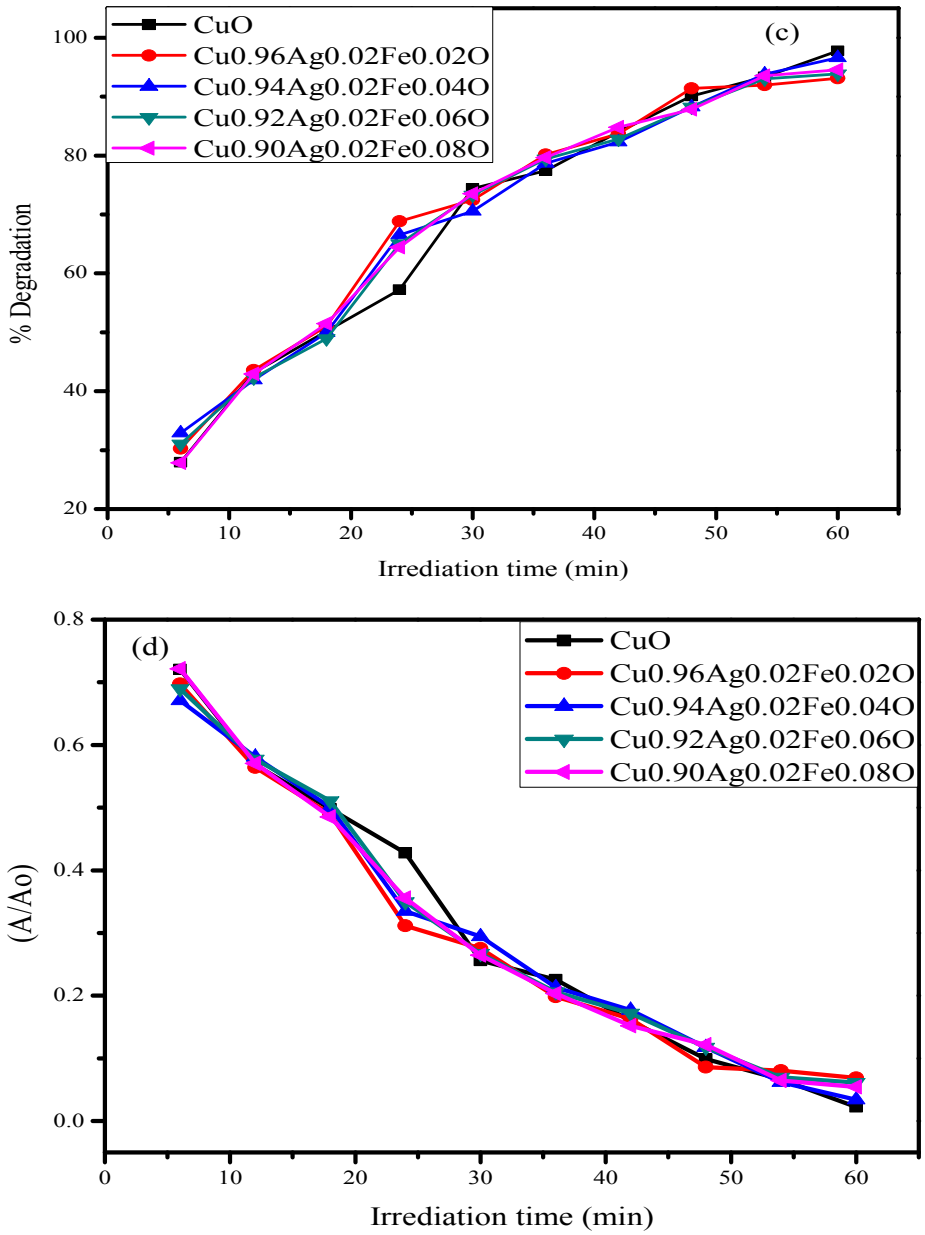

Figure 10 (*continued*). Percentage degradation **(a, c)** and catalytic efficiency **(b, d)** of undoped and (Ag, Fe) co-doped CuO NPs with different concentration of Fe (0.02, 0.04, 0.06 and 0.08 M) at same concentration of Ag content (0.02 M).

activity than the all other concentration of co-doped CuO NPs. Furthermore, $Cu_{0.94}Ag_{0.02}Fe_{0.04}O$, $Cu_{0.92}Ag_{0.02}Fe_{0.06}O$ and $Cu_{0.90}Ag_{0.02}Fe_{0.08}O$ NPs samples showed a lower percentage of degradation of MB dye than $Cu_{0.96}Ag_{0.02}Fe_{0.02}O$ NPs sample.

Table 5 and 6 shows that the rate of degradation of MO and MB dye decreases with co-doping of (Ag, Fe) on pure CuO NPs at different concentrations. This happened due to particle size, crystal structure and shapes of synthesized NPs [51]. Pure CuO NPs reveal improved photocatalytic activity differentcompared with further prepared samples of (Ag, Fe) co-doped CuO NPs as evident from Tables 5 and 6. The photocatalytic activity depends on some basic parameters, which are the concentration of substrate, amount of photocatalyst, pH of

the solution, temperature of reaction medium, time of irradiation of light, the intensity of light, surface area of photocatalyst, dissolve oxygen in the reaction medium, nature of the photocatalyst, nature of the substrate, doping of metal ions and non-metal and structure of photocatalyst and substrate. This is due to the reason that concentration of dopants in CuO lattice and the structure of the synthesized NPs. $Cu_{0.96}Ag_{0.02}Fe_{0.02}O$ should have a high photocatalytic activity, such as co-dopants can be easily incorporated into the crystal lattice of CuO because of their similar ionic radii of host CuO. The degradation of dyes is usually faster in mixed systems than single systems because the oxidation of dyes consumes photo-excited holes promptly and efficiently, thus attenuating electron-hole recombination. In the case of another dopant concentration, the amount of photocatalyst should be take the low amount of photocatalyst (less concentration of dopants and Cu ions). The photodegradation also decreased in comparison to $Cu_{0.96}Ag_{0.02}Fe_{0.02}O$. The researchers also reported the same trends for photocatalytic activities for chromium doped Cobalt Oxide (Cr) Co_3O_4 NPs and CuO/TiO_2 nanocomposites [51, 52].

The photocatalytic activity of any photocatalyst is much affected by the bandgap values of synthesized NPs. The bandgap values of NPs are more significant; this is due to the slower electron-hole recombination rate. Consequently, electrons and holes generated in the bulk are allowed to reach the photocatalyst surface and participate in the photoreactions. Therefore, it is expected here that undoped CuO NPs have better photocatalytic activity than those of (Ag, Fe) co-doped CuO NPs. However, the other factors that influence recombination rate between the holes and the electrons are- crystal size, surface area, defect population, and porosity. Therefore, any difference in these characteristics for CuO and (Ag, Fe) co-doped CuO NPs preserve results in a significant alteration in their photocatalytic activity. We predict that undoped CuO NPs (30 mg) for MO and MB dye is an effective photocatalytic activity (percentage of degradation of dye as 85 % and 97 %) since it reduces the direct and indirect band gap values 1.42 eV and 1.28 eV, $Cu_{0.96}Ag_{0.02}Fe_{0.02}O$ NPs (30 mg) for MO and MB have a percentage of degradation of dye as 73 % and 93 %, in this case, the values of direct and indirect band gap are 1.45 eV and 1.04 eV, $Cu_{0.94}Ag_{0.02}Fe_{0.04}O$ NPs (30 mg) for MO and MB have a percentage of degradation of dye as 84 % and 96 %, in this case, the values of direct and indirect band gap are 1.54 eV and 1.51 eV, $Cu_{0.92}Ag_{0.02}Fe_{0.06}O$ NPs (30 mg) for MO and MB have a percentage of degradation of dye as 79 % and 93 %, in this case, the values of direct and indirect band gap are 1.54 eV and 0.69 eV and $Cu_{0.90}Ag_{0.02}Fe_{0.08}O$ NPs (30 mg) for MO and MB have 81 % and 94 %, in this case, the values of direct and indirect band gap are 1.54 eV and 0.69 eV. These results indicate that the MB dye showed a better percentage of degradation of dyes at 30 mg of concentration of NPs as compared to MO dye. Thus, pure CuO NPs have more efficient photocatalytic activity as compared to co-doped CuO NPs.

6. Conclusions

Undoped and (Ag, Fe) co-doped CuO NPs with different content of Fe (0.02, 0.04, 0.06 and 0.08 M) at the same range of Ag (0.02 M) have been fabricated through microwave-assisted scheme. In this paper, the results revealed that (Ag, Fe) co-doping extensively affected the structural, morphological and optical properties of pure NPs. The structural properties of NPs are well-known by XRD and FESEM. The average crystallite sizes of both undoped and co-doped CuO NPs are established in 13-24 nm. SEM and EDX results also assert high purity and unusual morphologies of NPs. From HR-TEM patterns, the particle size of NPs found to be 19-21 nm. The direct and indirect bandgap values for co-doped CuO NPs are 1.41-1.54 eV and 0.69-1.51 eV. From the bandgap, results received that values of optical band gap for co-doped CuO NPs better as compared to undoped CuO NPs. FTIR results authenticate the configuration of Cu-O stretching in undoped and co-doped CuO NPs. Antibacterial activities of undoped CuO NPs are more significant in B. subtilis as compared to co-doped CuO NPs, but in the case of other bacterial strains (*S. aureus, E. coli)*, co-doped CuO NPs show the good antibacterial activity as compared to the undoped ones. Doping in NPs conducted great prospects for improvement in antimicrobial materials for antibiotic-free, bactericidal applications. Pure CuO NPs exhibit enhanced photocatalytic activity as compared to other synthesized (Ag, Fe) co-doped CuO NPs.

7. Conflicts of Interest

There are no conflicts of interest for the publication of this research article.

8. Acknowledgement

The authors are obliged to Career Point University Hamirpur, HP, to provide all possible help to conduct this research work.

References

1. L.V. Devi, T. Selvalakshmi, S. Sellaiyan, A. Uedono, K. Sivaji, S. Sankar, Effect of La Doping on the Lattice Defects and Photoluminescence Properties of CuO, *J. Alloy Compd*. 709 (2017) 496-504.
2. Z. H. Ibupoto, A. Tahira, H. Raza, G. Ali, A. A. Khand, N. S. Jilani, A. B. Mallah, C. Yu, M. Willander,Synthesis of Heart/Dumbbell-Like CuO Functional Nanostructures for the Development of Uric Acid Biosensor. *Mater.* 11 (2018) 2-13.
3. H. R. Naika, K. Lingaraju, K. Manjunath, D. Kumar, G. Nagaraju, D. Suresh, H. Nagabhushana, Green Synthesis of CuO Nanoparticles using *Gloriosa superba* L. Extract and their Antibacterial Activity. *J. Taibah Univ. Sci.* 9 (2015) 7-12.
4. A. Balkrishna, A. Kumar, V. Arya, A. Rohela, R. Verma, E. Nepovimova, O. Krejcar, D. Kumar, N. Thakur, K. Kuca. Phytoantioxidant Functionalized Nanoparticles: A Green Approach to Combat Nanoparticle-Induced Oxidative Stress. *Oxid. Med. Cell. Longev.* 2021 (2021).
5. L. Attou, B. Jaber, H. E. Zahraouy, Effect of Annealing Temperature on Structural, Optical and Photocatalytic properties of CuO Nanoparticles, *Mediterr. J. Chem.* 7 (2018) 308-316.
6. Anu, N. Thakur, J. Kumar, Synthesis and characterization of pure and Zn-doped copper oxide. *Int. J. Adv. Eng.* 7 (2018) 1-5.
7. N. Thakur, Anu, K. Kumar, A. Kumar, Effect of (Ag, Zn) co-doping on structural, optical and bactericidal properties of CuO nanoparticles synthesized by a microwave-assisted method. *Dalton Trans.* 50 (2021) 6188-6203.
8. K. A. Mishjil, K. Qader, W. A. Jabber, Z. A. Toma, Study the Effect of Mn-doped CuO Thin Film on its Optical Properties, *Mater. Sci. Ind. J.* 13(2015) 389-392.
9. F. Teng, W. Yao, Y. Zheng, Y. Ma, Y. Teng, T. Xu, S. Liang, Y. Zhu, Synthesis of Flower-like CuO Nanostructures as a Sensitive Sensor for Catalysis, *Sensor. Actuat. B* 134 (2008) 761-768.
10. A. M. E Sayed, M. Shaban, Structural, Optical and Photocatalytic Properties of Fe and (Co, Fe) co-doped Copper Oxide Spin Coated Films, *Spectrochim. Acta A Mol. Biomol. Spectrosc.*149 (2015) 638-646.
11. Y. Gulen, F. Bayansal, B. Sahin, H.A. Cetinkara, H.S. Guder, Fabrication and characterization of Mn-doped CuO thin films by the SILAR method, *Ceram. Int.* 39 (2013) 6475-6480.
12. A. Suganthi, S. J. K. Vethanathan, S. Perumal, D. P. Koilpillai, S. Karpagavalli, Optical and Electrical Properties of Solvothermally Synthesized Manganese Doped Cuprous Oxide Nanoparticles, *IOSR J. Appl. Phy.* 1 (2017) 43-48.
13. K. Kannan, D. Radhika, S. Vijayalakshmi, K. K. Sadasivuni, A. A. Ojiaku, U. Verma, Facile Fabrication of CuO Nanoparticles via Microwave Assisted Method: Photocatalytic, Antimicrobial and Anticancer Enhancing Performance, *Int. J. Environ. Anal. Chem.* (2020) 1-14.
14. Anu, N. Thakur, K. Kumar, K. K. Sharma, Application of Co-doped Copper Oxide Nanoparticles Against Different Multidrug Resistance Bacteria, *Inorg. Nano-Metal Chem.* (*2020)* 1-12.
15. N. M. Basith, J. J. Vijaya, L. J. Kennedy, M. Bououdina, Structural, Morphological, Optical, and Magnetic Properties of Ni Doped CuO Nanostructures Prepared by a Rapid Microwave Combustion Method, *Mat. Sci. Semicon. Proc.* 17 (2014) 110-118.
16. H. Khmissi, A. M. E. Sayed, M. Shaban, Structural, Morphological, Optical Properties and Wettability of Spin-coated Copper Oxide, Influences of Film Thickness, Ni, and (La, Ni) co-doping, *J. Mater. Sci. 5*1 (2016) 5924-5938.
17. A. Balkrishna, V. Arya, A. Rohela, A. Kumar, R. Verma, D. Kumar, E. Nepovimova, K. Kuca, N. Thakur, N.

Thakur, P. Kumar. Nanotechnology Interventions in the Management of COVID-19: Prevention, Diagnosis and Virus-Like Particle Vaccines. *Vaccines* 9 (2021) 1129.

18. F. Bayansal, T. Taskopru, B. Sahin, H. A. Cetinkara, Effect of Cobalt Doping on Nanostructured CuO Thin Films, *Metall. Mater. Trans. A*, 45A (2014), 3671-3674.
19. G. Viruthagiri, E. Gopinathan, N. Shanmugam, R. Gobi, Synthesis and Characterization of ZrO_2-CuO co-doped Ceria Nanoparticles via Chemical Precipitation Method, *Spectrochim. Acta A Mol. Biomol. Spectrosc.* 131 (2014) 556-563.
20. S. M. Yakout, A. M. El-Sayed, Structural, Morphological and Ferromagnetic Properties of Pure and (Mn, Co) codoped CuO Nanostructures. *J. Supercond. Nov. Magn.* 29(2016), 2961-2968.
21. Y. Lv, L. Li, P. Yin, T. Lei, Synthesis and Evaluation of the Structural and Antibacterial Properties of Doped Copper Oxide. Dalton Trans. 49 (2020) 4699-4709.
22. C. Khatana, A. Kumar, M. W. Alruways, N. Khan, N. Thakur, D. Kumar, A. Kumar. Antibacterial Potential of Zinc Oxide Nanoparticles Synthesized using Aloe vera (L.) Burm. f.: A Green Approach to Combat Drug Resistance. *J. Pure Appl. Microbiol.* 15 (2021) 1907-1914.
23. A. Azam, A. S. Ahmed, M. Oves, M., M. S. Khan, A. Memic, Size-dependent Antimicrobial Properties of CuO Nanoparticles against Gram-positive and-negative Bacterial Strains. *Int. J. Nanomedicine*. 7 (2012) 1-8.
24. R. Dadi, R. Azouani, M. Traore, C. Mielcarek, Kanaev, A, Antibacterial Activity of ZnO and CuO Nanoparticles against Gram positive and Gram negative Strains. *Mater. Sci. Eng. C*, 104 (2019) 109968.
25. N. Dasineh Khiavi, R. Katal, S. Kholghi Eshkalak, S, Masudy-Panah, S. Ramakrishna, H. Jiangyong, Visible light driven heterojunction photocatalyst of CuO–Cu2O thin films for photocatalytic degradation of organic pollutants. *Nanomater.*, *9*(2019), 2-12.
26. P. Kar, K. Shukla, P. Jain, R. K. Gupta, An activated carbon fiber supported Fe 2 O 3@ bismuth carbonate heterojunction for enhanced visible light degradation of emerging pharmaceutical pollutants. *Reac. Chem. Engineer.,* 6(2021), 2029-2041.
27. B. Balasubramaniam, N. Singh, P. Kar, A. Tyagi, J. Prakash, R. K. Gupta, Engineering of transition metal dichalcogenides-based 2D nanomaterials through doping for environmental applications. *Mol. Syst. Des. Eng.,* **4(2019),** 804-827.
28. P. Kar, P. Jain, V. Kumar, R. K. Gupta, Interfacial engineering of Fe2O3@ BOC heterojunction for efficient detoxification of toxic metal and dye under visible light illumination. *J. Environ. Chem. Eng.*, *7*(2019), 102843.
29. B. Sharma, S. Thakur, G. Mamba, R. K. Gupta, V. K. Gupta, V. K. Thakur, Titania modified gum tragacanth based hydrogel nanocomposite for water remediation. *J. Environ. Chem. Eng.*, *9*(2021), 104608.
30. P. Jain, A. Kumar, N. Verma, R. K. Gupta, In-situ synthesis of TiO_2 nanoparticles in ACF: Photocatalytic degradation under continuous flow. *Solar Energy*, 189 (2019), 35-44.
31. N. Singh, R. Chakraborty, R. K. Gupta,. Mutton bone derived hydroxyapatite supported TiO2 nanoparticles for sustainable photocatalytic applications. *J. Environ. Chem. Eng.*, *6*(2018) 459-467.
32. T. S. Vijayakumar, S. Karthikeyeni, S. Vasanth, A. Ganesh, G. Bupesh, R. Ramesh, M. Manimegalai, P. Subramanian, Synthesis of Silver-Doped Zinc Oxide Nanocomposite by Pulse Mode Ultrasonication and its Characterization Studies, *J. Nanosci.* (2013) 1-7.
33. R. Gupta, N. K. R. Eswar, J. M. Modak, G. Madras, Ag and CuO impregnated on Fe doped ZnO for Bacterial Inactivation under Visible Light, *Catal. Today* 300 (2017) 71-80.
34. S. Sharma, K. Kumar. Aloe-vera leaf extract as a green agent for the synthesis of CuO nanoparticles inactivating bacterial pathogens and dye. *J. Dispers. Sci. Technol.* 42 (2021) 1950-1962.
35. S. Sharma, K. Kumar, N. Thakur, S. Chauhan, M. S. Chauhan. Eco-friendly Ocimum tenuiflorum green route synthesis

of CuO nanoparticles: Characterizations on photocatalytic and antibacterial activities. J. Environ. Chem. 9 (2021) 105395.

36. A. P. kumar, N. S. kumar, K. C. M. G. Malar, M. Meena, I. V. Potheher, A Comparative Analysis on the Dye Degradation Efficiency of pure, Co, Ni and Mn-doped CuO Nanoparticles, *J. Mater. Sci. Mater. Electron.* (2019) 1-17.
37. D. Djouadi, O. Slimi, L. Hammiche, A. Chelouche, T. Touam. Effects of (Ce, Cu) Co-doping on the Structural and Optical Properties of ZnO Aerogels Synthesized in Supercritical Ethanol. *J. Phys.: Conf. Ser.* 987 (2018) 1-10.
38. A. Bakravi, Y. Ahamadian, H. Hashemi, H. Namazi, Synthesis of Gelatin-Based Biodegradable Hydrogel Nanocomposite and their Application as Drug Delivery *Agent. Adv. Polym. Technol.* 37 (2018) 2625-2635.
39. N. Thakur, Anu, K. Kumar, Effect of (Ag, Co) Co-doping on the Structural and Antibacterial Efficiency of CuO Nanoparticles: A Rapid Microwave Assisted Method, *J. Environ. Chem. Eng.* 8 (2020) 1-9.
40. J.D. Visurraga, C. Daza, C. Pozo, A. Becerra, C. V. Plessing, A. Garcia, Study on Antibacterial Alginate-Stabilized Copper Nanoparticles by FT-IR and 2D-IR Correlation Spectroscopy, *Int. J. Nanomed.* 7 (2012) 3597-3612.
41. A. A. Radhakrishnan, B. B. Beena, Structural and Optical Absorption Analysis of CuO Nanoparticles, *Ind. J. Adv. Chem. Sci.* 2 (2014) 158-161.
42. S. Dhanuskodi, M. Manikandan, K. Karthik, Structural, Optical and Dielectric Properties of Fe Doped CuO Nanoparticles,*Proceedings of National Laser Symposium (NLS-22), Manipal University, Manipal,* (2014) 8-11.
43. L. S. Miller,. Electron Energy Bands. *Electr. Mater*., *Springer, Boston*, MA, 9-17.
44. S. Sharma, K. Kumar, N. Thakur, S. Chauhan, M. S. Chauhan, The effect of shape and size of ZnO nanoparticles on their antimicrobial and photocatalytic activities: a green approach, *Bull. Mater. Sci.* 43 (2020) 1-10.
45. S. Sharma, K. Kumar, N. Thakur, M.S. Chauhan, Ocimum Tenuiforum leaf extract as a green mediator for the synthesis of ZnO nanocapsules inactivating bacterial pathogens, *Chemical Papers*, 50 (2020) 1-11.
46. S. Sharma, K. Kumar, N. Thakur. Green synthesis of silver nanoparticles and evaluation of their anti-bacterial activities: use of Aloe barbadensis miller and Ocimum tenuiflorum leaf extracts. *Nanofabrication*, 6 (2021), 52-67.
47. M. Saraf, M. Tavakkoli Yaraki, Prateek, Y. N. Tan, Y.N. , R. K. Gupta, Insights and Perspectives Regarding Nanostructured Fluorescent Materials toward Tackling COVID-19 and Future Pandemics. *ACS Appl. Nano. Mater. 4*(2021), 911-948.
48. Z. Usmani, T. Lukk, D. K. Mohanachandran, V. K. Thakur, V.K. Gupta, D. Robert, J. Raj, F. Scarpa, R.K. Gupta, Biosafe sustainable antimicrobial encapsulation and coatings for targeted treatment and infections prevention: Preparation for another pandemic. *Curr. Res. Green. Sustainable. Chem.*, 4(2021), 1-5.
49. B. Balasubramaniam, Prateek, S. Ranjan, M. Saraf, P. Kar, S. P. Singh, V. K. Thakur, A. Singh, R. K. Gupta, Antibacterial and antiviral functional materials: Chemistry and Biological Activity toward Tackling COVID-19-like Pandemics. *ACS Pharmacol. Translat. Sci., 4*(2021), 8-54.
50. N. Thakur, N. Thakur, V. Bhullar, S. Sharma, A. Mahajan, K. Kumar, D. Pathak, TiO_2 nanofibers fabricated by electrospinning technique and degradation of MO dye under UV light, *Z. Kristallogr. Cryst. Mater.* 236 (2021), 239-250.
51. G. Hitkari, S. Sandhya, P. Gajanan, M. K. Shrivash, D. Kumar, Synthesis of Chromium Doped Cobalt Oxide (Cr: Co3O4) Nanoparticles by Co-Precipitation Method and Enhanced Photocatalytic Properties in the Visible Region, *J. Mater. Sci. Eng*. 7 (2018), 2-6.
52. T. N. M. Ravishankar, D. O. Vaz, S. R. Teixeira, The Effects of Surfactant in the sol-gel Synthesis of CuO/TiO_2 Nanocomposites on its Photocatalytic Activities under UV-visible and visible light illuminations, *New J. Chem.* 44 (2020) 1888-1904.